Check for updates

Recent research progress on polyoxometalate-based electrocatalysts in energy generation

Kai Li,[a] Tao Liu,[b] Jun Ying, [ID] *[a] Aixiang Tian [ID] [a] and Xiuli Wang [ID] *[a]

Sustainable energy generation is a pressing challenge in the society today, driven by the rapid exponential growth in industrialization. Thus, it has become an urgent priority to find sustainable solutions for energy generation. Polyoxometalates (POMs) are a class of materials characterized by diverse components, which provide numerous active sites, electronic regulatory effects, synergistic effects, structural diversity, and controllability. Researchers have made remarkable progress in regulating the catalytic performance of POM-based electrocatalysts by improving the configuration of POMs. Herein, we aim to review the recent research progress (from 2020 to present) on the relation between different types of POMs and their catalytic activities in electrocatalytic oxygen evolution (OER), electrocatalytic hydrogen evolution (HER) and CO_2 reduction (CO_2RR). By analyzing the application of POMs in different electrocatalytic fields, the suitability of POMs in these areas can be further determined and possible specific explanations can be summarized. The most important aspect is to provide relevant guidance for future researchers in the synthesis of POM-based electrocatalysts, where their electrocatalytic performance can be improved to the maximum extent through the reasonable selection of POMs. The utilization of POM-based electrocatalysts shows tremendous promise to address the pressing issues related to energy scarcity, providing a pathway to realize sustainable energy generation.

[a]*College of Chemistry and Materials Engineering, Bohai University, Jinzhou 121013, P. R. China. E-mail: ying@bhu.edu.cn; wangxiuli@bhu.edu.cn*

[b]*College of Sciences, North China University of Science and Technology, Tangshan, Hebei 063210, China*

1. Introduction

Energy is of utmost importance in achieving sustainable development in society. Currently, approximately 80% of the global energy demand is met by fossil fuels, which face the risk of depletion.[1] Thus, gradually transitioning from fossil fuels to sustainable and pollution-free non-fossil energy sources has

Kai Li received his Bachelor's degree from Bohai University in 2022 and currently is studying for his Master's degree under the guidance of Associate Professor Jun Ying of Bohai University. His research interests focus on (1) the synthesis of POM-based fluorescent probes for heavy metal ion monitoring and (2) the synthesis and application of POM-based electrocatalysts.

Kai Li

Jun Ying received his Bachelor's degree from Hebei Normal University in 2004, his Master's degree in 2009 under the guidance of Professor Bin Li of Northeast Normal University, and his Doctorate in 2019 under the guidance of Professor Yaguang Chen of Northeast Normal University. Since his graduation, he has been working as an Associate Professor at Bohai University. His current research interests mainly

Jun Ying

include (1) the synthesis of POM-based fluorescent probes for heavy metal ion monitoring; (2) the synthesis and application of POM-based electrocatalysts; and (3) the synthesis application of POM-based viologen hybrid materials.

become an inevitable development trend. According to market research institutions, the global hydrogen (H_2) energy market reached around 90 billion US dollars in 2023, marking a 10% increase compared to 2022.[2] Nevertheless, the majority of H_2 production worldwide still relies on methods such as steam reforming and partial oxidation of hydrocarbons, which leads to significant carbon dioxide (CO_2) emission.[3,4] As reported by the International Energy Agency (IEA), the global energy-related CO_2 emission is projected to reach 36.8 billion tons, reflecting a 1.1% increase compared to 2022.[5] In view of this situation, the most effective and fundamental approach to address these challenges is to identify alternative renewable and clean energy sources that can meet global energy demands and facilitate the efficient transformation and utilization of CO_2.[6]

The energy crisis stems from the excessive dependence on fossil fuels and thus needs immediate attention, emphasizing the importance of utilizing renewable energy and promoting efficient energy conversion technology.[7] Within this realm, electrochemical energy conversion has become a prominent field, especially in the domains of water splitting and CO_2 reduction (CO_2RR).[8,9] These technologies show considerable potential in generating clean and sustainable energy carriers.[10] Water splitting involves two types of redox reactions, hydrogen evolution reaction (HER) and oxygen evolution reaction (OER), which hold great potential for generating environmentally friendly H_2 and oxygen (O_2).[11,12] H_2 plays a crucial role in energy generation, particularly as a fuel source for electricity generation in fuel cells.[13] Fuel cells facilitate the reaction between H_2 and O_2, resulting in the production of water and the generation of electricity. This process is characterized by its clean and emission-free nature, making H_2 an environmentally friendly energy choice. Alternatively, the electrocatalytic reduction of CO_2 presents a promising avenue for the production of valuable carbon-based products. This process facilitates the effective recycling of natural carbon resources, fostering a circular and eco-friendly carbon economy. The resultant products include

C1 (CH_4, $HCOOH$, and CH_3OH) and C2 (C_2H_4, C_2H_6, and CH_3COOH) compounds.[14–17] However, considering the high activation barrier of this type of reaction, efficient electrocatalysts with multiple catalytic sites are important to promote the necessary proton-assisted multi-electron transfer process to synthesize the required oxidation and reduction products.[18]

Polyoxometalates (POMs) are a class of multicomponent ion clusters composed of metal (V^V, Mo^V, Nb^V, Ta^V, Mo^{VI} and W^{VI}) and oxygen atoms, possessing diverse structural and chemical properties.[19] POM molecules are formed by the connection of multiple metal centers and oxygen atoms through shared oxygen bridge bonds, resulting in stable spatial structures.[20] To date, a wide range of POM structures has been reported, exhibiting exceptional characteristics that make them highly versatile in various fields.
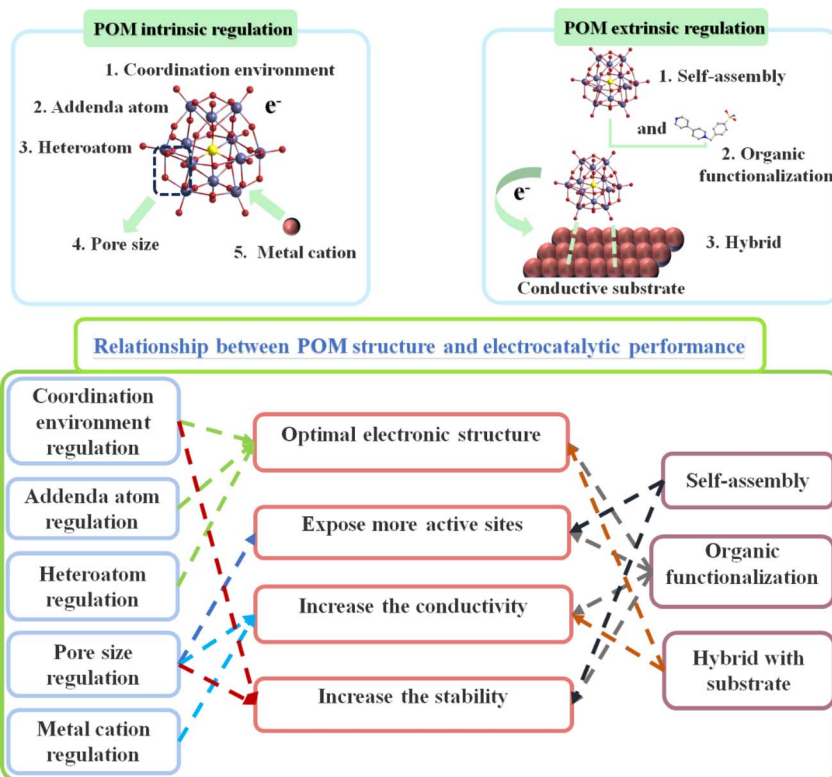
POMs possess a tunable chemical composition and structure, enabling the syntheses of POM-based compounds with different chemical properties and reactivity by adjusting the synthetic method.[21] POMs demonstrate excellent performance and stability, making them promising candidates for applications in covalent/coordination design and assembly of mixed organic–inorganic frameworks. By employing POMs as building blocks, interactions and assemblies with organic molecules can be achieved, facilitating the construction of composite materials with specific structures and properties.[22] This organic–inorganic hybrid framework extends the functions and properties of traditional materials, especially in the field of electrocatalysis. In the field of electrocatalysis, POM-based catalysts have demonstrated advantages through both intrinsic and extrinsic regulation strategies (Scheme 1). Here, we provide a specific summary of the advantages of POM-based electrocatalysts: (I) POM-based compounds consist of various metal ions and polyoxoanions, providing rich compositional and structural control. This allows for tuning their catalytic performance by adjusting their composition and structural parameters, enabling optimization for specific reactions.[23] (II) POMs possess abundant accessible active sites that can serve as catalytic centers for electrocatalytic reactions. Furthermore, their multi-metallic structure and highly dispersed ion coordination enable them to offer high activity and selectivity, resulting in an excellent performance in electrocatalytic reactions.[24] (III) POMs exhibit good stability in electrocatalytic reactions. Their multi-metallic structure and discrete ion coordination enable them to resist corrosion and structural degradation in oxidative, reductive, acidic, and alkaline environments, thus prolonging the service life of materials.[25] (IV) The structural parameters of POMs can be precisely controlled by adjusting their composition, topology, and pore structure. This tunability enables the customized design of POMs to meet the specific requirements of electrocatalytic reactions, leading to an optimal catalytic performance.[26] Based on the aforementioned advantages, POM-based compounds have demonstrated potential as efficient electrocatalysts for energy generation. For instance, POMs exhibit remarkable catalytic activity and selectivity for crucial processes such as OER and HER involved in water splitting and CO_2RR (Scheme 2).[11,23] Moreover, POMs exhibit significant
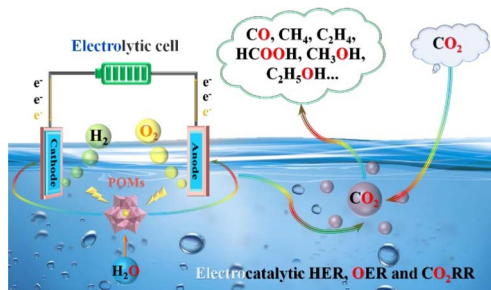
Xiuli Wang

Xiuli Wang received her Master's degree in Inorganic Chemistry from Northeast Normal University in 1996. From 2000 to 2003, she pursued her doctoral degree at the Institute of Polyoxometalate Chemistry of Northeast Normal University. Subsequently, she went directly to Nankai University to pursue a postdoctoral degree after completing her doctorate in 2003. At present, she is the President of Bohai University Institute of Chemistry and Materials Engineering and is recognized as an outstanding talent in Bohai University. Her current research interests include (1) the synthesis and fluorescent properties of novel POM-based complexes and (2) the synthesis and application of POM-based catalysts.

Scheme 1 Relationship between structure control strategy and electrocatalytic performance of POM-based electrocatalysts.

Scheme 2 POM-based electrocatalysts for efficient electrocatalytic applications (HER, OER and CO_2RR).

promise in reducing CO_2 emissions, given that they can convert greenhouse gases into valuable fuels and chemicals.[24]

It is well known that electrocatalytic reactions such as HER, OER, and CO_2RR are reduction reactions, and the active sites for these reactions are typically metal sites. However, enhancing the reaction activity of electrocatalysts by increasing the number of active sites has been a major challenge for researchers. In recent years, the introduction of POMs in electrocatalysts has become a focal point. (I) The introduction of POMs allows control of the morphology, particle size, and pore structure of the material, thereby increasing the specific surface area of the electrocatalyst.[25] A larger surface area means more exposed metal reaction sites, leading to improved activity in reduction reactions. (II) The structure of POMs is tunable, and

by removing a structural unit, appropriate coordination atoms and transition metals can be selected to regulate their structure. Optimized structures can increase the number and activity of exposed metal reaction sites, thereby improving the efficiency of reduction reactions.[26] (III) The presence of auxiliary heteroatoms such as nitrogen and sulfur in the material can alter the electronic structure and surface chemistry of POMs, enhancing the activity of the metal reaction sites. These auxiliary heteroatoms can create synergistic effects with metal atoms, promoting reduction reactions.[27] (IV) Introducing modifying groups or functional groups on the surface of POMs can increase the surface active sites of the material.[28] These groups can adsorb target reduction reactants, provide additional reduction reaction sites, and improve the interaction between the material and reactants.

Different from previous reviews, this review provides a detailed classification of POM-based electrocatalysis into POM-based single-crystal structures and POM-based nanostructures, providing a comprehensive overview of the electrocatalytic mechanisms and challenges in HER, OER, and CO_2RR. More importantly, the suitability of POMs in these areas can be further determined by analysing their applications in different electrocatalytic fields. Based on the summarized possible explanations, the rational selection of POMs can maximize the electrocatalytic performance. Finally, this review systematically discusses the advantages, challenges, strategies, and prospects of POM-based electrocatalysts, which are crucial for the development of electrocatalysis in energy generation.

2. Development of POM-based electrocatalysts

2.1 Fundamental structures and redox activities of POMs

POMs are a type of anionic metal oxide species primarily composed of redox active metal centers.[25] These electron-deficient molecular units are formed through the condensation of basic oxygen anions. The most common unit is the tetravalent oxygen anion $[MO_4]_n$, which is connected in the form of $\{MO_n\}$ in acidic media.[26] POMs have emerged as highly attractive molecular catalysts and redox mediators, finding applications in catalytic systems involving multi-electron or multi-proton transfer.[27–30] A deep understanding of the intrinsic properties of the original POMs is crucial for optimizing their electrocatalytic performance. It is essential to firmly grasp key concepts related to the original POMs, such as classical POM structure, structural evolution, composition adjustment and redox behavior, to rationally design suitable POM-based electrocatalysts for practical applications.

2.1.1 Background of POM configuration development.
In 1934, British physicist Keggin proposed the renowned Keggin structure model through experiments by utilizing powder X-ray diffraction (PXRD).[31] Furthermore, Keggin-type POMs continue to be the most widely synthesized, extensively researched and promising class of POMs to date. The classic Keggin-type POMs, including $H_3PW_{12}O_{40}$, $H_3PMo_{12}O_{40}$, $H_4SiW_{12}O_{40}$ and $H_4SiMo_{12}O_{40}$, have found widespread applications in industrial production due to their well-established systems.[32–35] Dawson-type POMs represent another crucial category of POMs with a structure similar to Keggin-type POMs. These POMs were initially discovered by American chemist Edgar Fahs Smith in 1926 and named after fellow American chemist Arthur A. Dawson. Further research on Keggin and Dawson-type POMs revealed the existence of sandwich-type POM structures. These structures consisted of two Keggin or Dawson-type POMs and a tetranuclear transition metal cluster and were named "Finke" structures.[36] Subsequent in-depth studies revealed other hetero-POM structures and iso-POM structures with different X/M ratios, such as Anderson $[XM_6O_{24}]^{n-}$, Lindqvist $[M_6O_{19}]^{n-}$, Evans–Showell $[Co_2Mo_{10}H_4O_{38}]^{6-}$, isopolymolybdates $[Mo_8O_{26}]^{4-}$, and isopolyvanadates $[V_{10}O_{28}]^{6-}$ (Fig. 1a).[37–41]

Due to the pH-sensitive nature of POM structures, it is possible to construct isomers and vacancy-type POMs by modifying the $\{MO_6\}$ building blocks. The Keggin structure has five Baker–Figgis isomers (α, β, γ, δ, and ε), which are distinguished by the different rotation directions and angles of the trimeric metal clusters that constitute their primary structure.[42] The derivative structures of Keggin-type POMs are constructed by removing one or more $\{MO_6\}$ building blocks, creating one or more vacancies that can accommodate external metal ions.[43] Furthermore, the heteroatom at the center of POMs can be substituted with other elements, while maintaining their crystal structure (Fig. 1b). This characteristic makes POMs a versatile series of molecular clusters that can modify their structure and properties in response to various external stimuli.[44] The unique structural distribution formed after substitution with new heteroatoms and introduction of metal ions can contribute to improved electrochemical performances.[45]

2.1.2 The relationship between structure and redox activity of POMs.
The electronic structure and redox properties of POMs can be precisely tuned by modifying their building blocks. Specifically, these modifications involve changing the structural
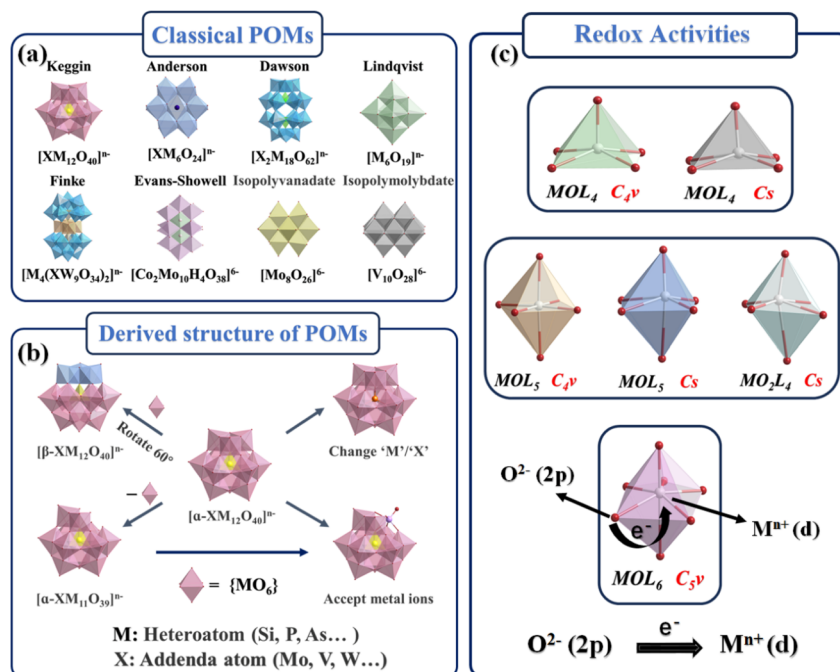

Fig. 1 (a) Polyhedral structure view of classical POM types. (b) Conversion of Keggin-type POM derivative system. (c) Different types of the polyhedral MO_xL_y of POMs and redox activities in POM structural unit.

This journal is © The Royal Society of Chemistry 2024

J. Mater. Chem. A, 2024, **12**, 13576–13604 | **13579**

units formed by the connection between the central metal (Mo/W) and oxygen.[46] The reversible or irreversible redox activity of POMs is typically attributed to the electron transfer occurring from the terminal oxygen (O^{2-}) of their building units to the empty and non-bonding d orbitals of their metal centers.[47] The metal–oxygen structural units can be categorized into several types (Fig. 1c). The first type features POM structural units with pyramid-shaped MOL_4, which is commonly based on vanadium and possesses hollow structures. These hollow structures serve as storage sites for anions such as CO_3^{2-}, Cl^-, and I^-.[48] These POMs exhibit remarkable ability to undergo numerous consecutive single-electron exchanges in organic media. This unique feature allows them to facilitate electron transfer processes with exceptional efficiency. The second type is comprised of POMs represented by MOL_5 with C_{4v} symmetry. The metal centers (mainly Mo^{6+} or W^{6+}) are connected to a single non-shared oxygen atom at an octahedral position. Examples of this family include Keggin $[XM_{12}O_{40}]^{n-}$, Dawson $[X_2M_{18}O_{62}]^{n-}$ and Lindqvist $[M_6O_{19}]^{n-}$.[30,35,38] The terminal oxygen atoms coordinated to metal centers in their highest oxidation states usually exhibit redox capabilities. A substantial number of electrons can be delocalized on the metal atoms by undergoing a reduction process, leading to the formation of mixed-valence POMs. The third type consists of MO_2L_4 with C_s symmetry, corresponding to building blocks formed by additional atoms with two *cis* M=O bonds. These POMs do not undergo reversible redox processes because their reduction involves adding electrons to antibonding orbitals, leading to significant structural rearrangement of the polyanions. A representative example is the Anderson-type POMs or heptamolybdate $[Mo_7O_{24}]^{6-}$.[49] The fourth type is comprised of MO_2L_4 with C_s symmetry and MOL_5 with C_{4v} symmetry. These structural units exhibit reversible redox activity similar to MOL_5 with C_{4v} symmetry. The presence of abundant vacant sites allows them to coordinate various transition metals and oxygen-containing moieties, resulting in POMs with strong catalytic activity. Representative examples include vacant Keggin-type POMs ($[XM_{11}O_{39}]^{n-}$, $[XM_9O_{34}]^{n-}$) and vacant Dawson-type POMs $[H_7P_8W_{48}O_{184}]^{33-}$.[50–52] The fifth type represents POM configurations with pentagonal bipyramidal, MOL_6 with C_{5v} symmetry. This type has been widely used in wheel-shaped Mo clusters, where mixed-valence Mo^V/Mo^{VI} states are present.[53] However, to date, despite the potential presence of mixed-valence metals in these POMs, their exploration remains challenging due to their intricate structure and complex mechanism.

2.2 POM-based single-crystal structures

POMs exhibit the ability to self-assemble or combine with other metal elements and small organic molecules, resulting in the formation of unique single-crystal structures.[54] Generally, conventional solution methods, hydrothermal methods, solvothermal methods, *etc.* are employed for the synthesis of POM-based single-crystal structures. It is worth noting that the utilization of POM-based single-crystal structures offers several notable advantages. Firstly, these structures enable a comprehensive analysis of the assembly and substitution sites within POMs through crystal structure determination, which provides valuable insights into the variations in their electronic properties and redox capability. Moreover, these structures play a vital role in comprehending the electron transfer pathways between the reactive sites of POMs and reactants involved in electrocatalytic processes. This understanding can be harnessed to design highly efficient electrocatalysts with a well-defined strategy. Simultaneously, there is a close correlation between POM-related structures and electrocatalytic performance. The interactions among multiple metal atoms in the cluster structure can regulate the selectivity of catalytic reactions.[55] Thus, by adjusting the electronic structure of these clusters, such as controlling the electron transfer and redistribution between metal atoms, the electron transfer steps and intermediate species in catalytic reactions can be modulated. Additionally, the cluster structure has a large surface area and abundant pore structures, which help to enhance the specific surface area of the electrocatalyst and the diffusion rate of the reactants.[56] Moreover, the stability of the cluster structure is crucial for maintaining the catalytic performance. An ideal coordination environment of POMs can suppress the disintegration of the cluster structure and the leaching of the metal atom, thereby extending the lifespan of the catalyst.[57] Based on these advantages, a diverse range of POM structures has been developed in this field, including giant clusters, transition metal-substituted POMs and POM-based organic–inorganic hybrids. Consequently, this section focuses on the selection and discussion of three representative POM-based single-crystal structures.

2.2.1 Giant clusters.
Giant clusters are large molecular clusters composed of multiple metal ions and polyoxoanions.[55] These clusters typically consist of tens to hundreds of metal ions and exhibit complex structures and diverse morphologies, which have sparked widespread interest. The formation of giant clusters involves intricate processes including the interactions and assembly of multiple metal ions and polyoxoanions. Due to the presence of multiple metal ions, these clusters can provide multiple active sites, thereby demonstrating high catalytic activity and selectivity (Fig. 2a).[56] In 2020, Bugnola *et al.* successfully replicated a fully inorganic iron–tungsten oxide capsule with a Keplerate structure based on previous reports, which was designated as $\{Fe_{30}^{III}W_{72}^{VI}\}$ (Fig. 3a).[57,58] In this colossal cluster, two $\{W_5\}$ pentagonal units (known as $\{(W)W_5\}$) were positioned at the vertices of the icosahedron, connected by 30 Fe^{III} centers spanning the icosahedron. These units were assembled through metal coordination bonds, forming an extensive inorganic framework. The $\{Fe_{30}^{III}W_{72}^{VI}\}$ cluster demonstrated exceptional aerobic oxidation capability at the cathode, which generated active Fe(v)=O intermediates during organic catalytic processes. It may also be potentially formed by rapid intramolecular electron transfer within the capsule containing bridging O–W–O units, giving rise to the formation of binuclear Fe(iv)=O species. These findings indicate that $\{Fe_{30}^{III}W_{72}^{VI}\}$ serves as a promising electrocatalyst for iron-based inorganic analogs. In addition, other giant clusters with a host–guest structure have been explored, such as $\{Fe_{10}P_4W_{32}\}$, $\{Mo_{124}Ce_4\}$, $\{Nb-288\}$,
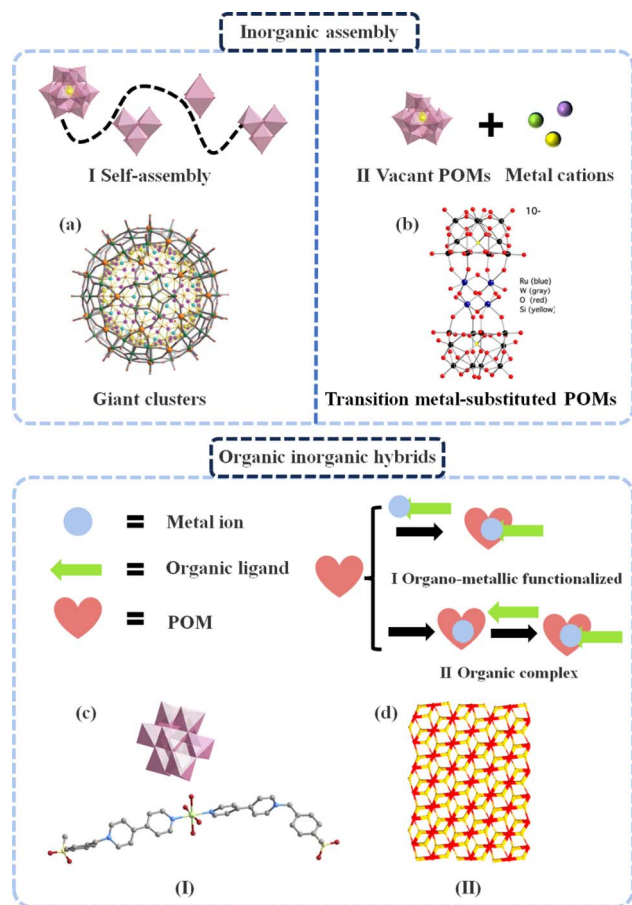
Fig. 2 Detailed composition of POM-based single-crystal structures. (a) Structure of giant POMs. Reproduced from ref. 57. Copyright 2010, WILEY-VCH Verlag GmbH & Co. KGaA, Weinheim. (b) Structure of substituted POMs. Reproduced from ref. 67. Copyright 2016, the American Chemical Society. Structure of organic inorganic hybrids: (c) organo-metallic functionalized and (d) organic complex. Reproduced from ref. 72. Copyright 2022, the American Chemical Society.
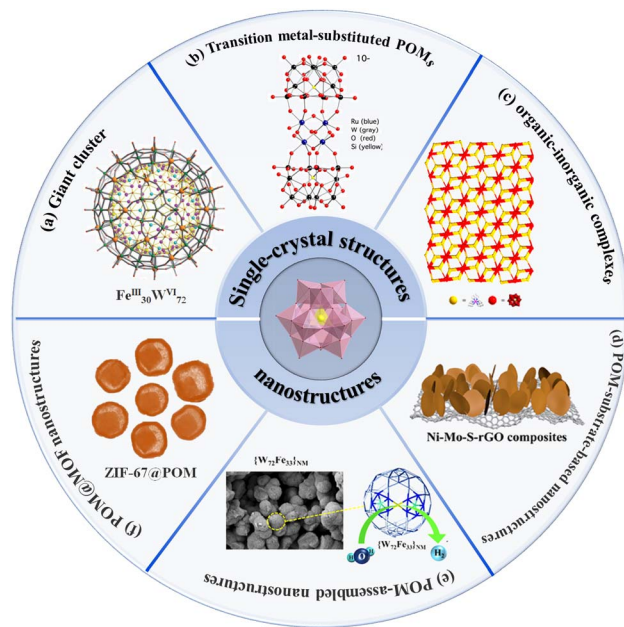

Fig. 3 Representative structure of POM-based electrocatalysts: (a) giant cluster. Reproduced from ref. 57. Copyright 2010, WILEY-VCH Verlag GmbH & Co. KGaA, Weinheim. (b) Transition metal-substituted POMs. Reproduced from ref. 67. Copyright 2016, the American Chemical Society. (c) POM-based organic–inorganic complexes. Reproduced from ref. 72. Copyright 2022, the American Chemical Society. (d) POM-substrate-based nanostructures. Reproduced from ref. 87. Copyright 2021, the American Chemical Society. (e) POM-assembled nanostructures. Reproduced from ref. 96. Copyright 2021, the American Chemical Society. (f) POM-encapsulated metal–organic framework nanostructures. Reproduced from ref. 98. Copyright 2019, the American Chemical Society.

and $\{Mo_{154}\}$.[59–62] These colossal structures exhibit various geometries resulting from the different coordination of the $\{MO_x\}$ units, leading to the coexistence of multiple oxidation states of metals within the molecules. This phenomenon facilitates reversible redox reactions during the catalytic process, making them promising representatives of electrocatalysts with great potential.

2.2.2 Transition metal-substituted POMs. Transition metal-substituted POMs (TM-POMs) refer to a class of compounds where transition metal ions are incorporated into the structure of POMs.[63] These POMs are typically composed of early-transition metals such as molybdenum and tungsten, which form a polyhedral core with oxygen atoms. The introduction of transition metal ions in the POM structure enables the tuning of their electronic, magnetic, and catalytic properties (Fig. 2b).[64–66] For example, Liu et al. synthesized a novel ruthenium-containing POM electrocatalyst, $[\{Ru_4O_4(OH)_2(H_2-O)_4\}(\gamma\text{-}SiW_{10}O_{36})_2^{10-}]$, aiming to achieve the efficient electrocatalytic oxidation of ethanol and methanol to aldehydes and acids by replacing tungsten on SiW_{12} with the transition metal

ruthenium (Fig. 3b).[67] Importantly, Ru^{IV} served as the true catalytic active center, which served as compelling evidence that the transition metal-substituted POMs possessed distinct electron distribution and electrocatalytic capabilities. The specific metal substitution and the surrounding POM framework play a crucial role in determining the catalytic performance of TM-POMs. The unique combination of redox properties of transition metals and the diverse reactivity of POM porous catalysts make TM-POMs highly promising in the fields of energy conversion and catalysis.

2.2.3 POM-based organic–inorganic hybrids. POM-based organic–inorganic hybrids are a class of materials that combine POMs with organic components, resulting in unique properties arising from the synergistic interaction between the inorganic POM cores and organic ligands (Fig. 2c and d).[68] POM-based organic–inorganic hybrids have attracted significant attention in various research fields, including catalysis, energy storage and materials science.[69–71] Tian et al. successfully synthesized three POM-based organic–inorganic hybrids, $[Co(phen)_3]_2[AsW_{12}O_{40}]\cdot 2H_2O$, $(Hbipy)_2[Mn(bipy)_3]_2[As_2W_{18}O_{62}]$ and $(H_2bib)_5[Co_4(H_2O)_2(AsW_9O_{34})_2]\cdot 2H_2O$, using a one-step hydrothermal synthesis method (Fig. 3c).[72] $(H_2-bib)_5[Co_4(H_2O)_2(AsW_9O_{34})_2]\cdot 2H_2O$ exhibited a sandwich structure of an arsenic tungstate supramolecular hybrid network,

which optimized its HER performance. Also, its exceptional capacitance and catalytic performance were attributed to the insertion of tetranuclear cobalt units, stable sandwich-type POM framework and abundant hydrogen bonding. These factors collectively provided additional redox centers and enhanced the electron transfer efficiency. POM-based organic–inorganic hybrids exhibit good stability and tunability, enabling the modulation of their catalytic activity and selectivity by changing the types and quantities of coordinating ions or ligands. As a result, POM-based organic–inorganic hybrids hold great promise in the field of electrochemical catalysis, offering hopeful solutions for critical applications such as sustainable energy conversion and storage.

2.3 POM-based nanostructures

POM-based nanostructures are a class of nanomaterials assembled using POMs as structural units. Due to their high stability, redox activity and tunable charge, POMs play a significant role in controlling the shape and enhancing the performance of nanomaterials.[73] POM-based nanostructures can be synthesized using various methods, such as solution-based synthesis, template-assisted fabrication and self-assembly.[74–76] Depending on the synthesis conditions and assembly techniques, the resulting POM-based nanostructures can exhibit different morphologies, including nanoparticles, nanowires, nanotubes and thin films.[77–80] Their size, shape and composition can be precisely controlled, enabling customized properties and functionalities. POM-based nanostructures serve as highly active electrocatalysts in various reactions due to their unique redox properties. Importantly, the synergistic effect between nanomaterials and POMs enhances their electrocatalytic performance, offering opportunities for innovation in the field of electrocatalysis. Their distinctive characteristics and controllable assembly provide opportunities for advancements in the field of electrocatalysis. Subsequently, several representative POM-based nanostructures will be introduced.

2.3.1 POM-substrate-based nanostructures. The controlled synthesis of POM-substrate-based nanostructures is an important approach for the design of POM-based nanocatalysts with good conductivity and tunable nanostructures.[81] In POM-substrate-based nanostructures, POMs can be incorporated into or onto various types of nanomaterials, such as metal nanoparticles, metal foam, metal oxides, metal sulfides and metal carbides.[82–86] The incorporation of POMs in nanomaterials can provide unique properties and functionalities in the resulting hybrid materials. The abundant oxygen atoms in POMs synergize with nanomaterials, functioning as active sites for electrocatalytic reactions. The strong/weak interactions between POMs and the nanomaterial substrate can modify the active centers, which lead to different levels of electron transfer, making POM-substrate-based nanostructures widely applicable in the field of electrocatalysis. Hou et al. published a study on the synthesis of a POM-based crystalline compound, $\{(trz)_3Ni_2 \cdot 6H_2O\}[H_3GeMo_{12}O_{40}]\cdot 9H_2O$ (trz = 1,2,4-triazole), as a precursor for POM-substrate-based nanostructures.[87] The authors employed the hydrothermal method to introduce sulfur

urea and graphene oxide (GO) in a high-pressure autoclave, resulting in the formation of Ni-Mo-S-rGO-200-24-2 nanocomposites (Fig. 3d). Moreover, this study highlighted the synergistic effect among Ni_3S_2, MoS_2, and reduced graphene oxide (rGO). The co-growth of Ni_3S_2 and MoS_2 led to modifications in the surface charge density of the nanosheets, creating more accessible catalytic active sites. The incorporation of rGO also contributed to an increase in the specific surface area of the electrocatalyst. Importantly, the utilization of the POM-based crystalline compound as a preassembled precursor resulted in the formation of Ni-Mo-S-rGO composites with uniformly distributed metal ions. In addition, extensive studies have been conducted on the utilization of substrate-based nanostructures. Liu et al. developed a novel catalyst for HER and OER by employing a POM (Co_2Mo_{10}) as the precursor and carbon paper as the carrier to fabricate CoMoS/FCP electrocatalysts.[88] The enhanced electrocatalytic activity of this material could be attributed to the larger surface area offered by the CoMoS/FCP nano-flower structure, as well as the effective activation of the MoS_2 active edges facilitated by Co atoms. Lu et al. employed Evans–Showell-type POM $\{Co_3[Co_2Mo_{10}O_{38}H_4]\}$ nanoclusters as precursors to synthesize a series of Co-promoted MoS_2-based nanosheets.[89] Subsequently, these nanosheets were assembled into an electrolytic cell for the purpose of overall water splitting. The introduction of the POM in the MoS_2 nanosheets resulted in a significant improvement in HER, particularly in alkaline media due to the reduction in the dissociation energy of water. Guillen-Soler et al. reported the synthesis of a distinct layered heterostructure consisting of POM/Pd/MoS_2, which exhibited great potential as an electrocatalytic material for water splitting.[90] The assembled POM/Pd/MoS_2 hybrid material incorporated POM as the OER catalyst, PdNP as the HER catalyst and MoS_2 flakes as the conductive matrix. The synergistic effect among these electroactive components endowed the hybrid material with strong electrocatalytic capability. These novel approaches circumvented the issue of disparate mesoporous structures that can arise from the use of multiple precursors with different nucleation rates. The homogeneous distribution of metal ions facilitates efficient electrocatalytic reactions and enhances the diffusion of electrolytes within the nanostructures.

2.3.2 POM-assembled nanostructures. The presence of POMs with a vast surface area, porosity, and tunable properties makes them highly attractive candidates for self-assembled nanostructures. During the self-assembly process, precise control of the size, shape, and composition of the nanostructures can be achieved, resulting in unique structures and properties.[91] Self-assembly involves the synergistic interaction of various driving forces, such as electrostatic interactions, hydrogen bonding, coordination bonding, solvent–solute interactions and other non-covalent interactions.[92–94] Factors such as the charge state, composition, and molecular structure of POM clusters, as well as the cationic effects of organic ligands, play crucial roles in the design and customization of POM-based nanostructures. Thus, it is necessary to carefully consider these factors to realize the required features and functions. Additionally, the incorporation of supplementary

13582 | J. Mater. Chem. A, 2024, **12**, 13576–13604

This journal is © The Royal Society of Chemistry 2024

functional nanostructures, such as nanoparticles or small organic molecules, into the POM matrix offers further opportunities for tailoring and customization.[95] This strategy allows the enhancement of specific properties or the introduction of new functionalities, expanding the potential applications of POM-based nanostructures. In recent years, POM-based cluster-assembled nanomaterials have found extensive applications in the field of electrocatalysis. In 2021, Kolli *et al.* combined the concept of Liu and Mu, and utilized a self-assembly approach to irreversibly assemble the crystalline compound $[Mo_{72}Fe_{30}O_{252}(CH_3COO)_{12}\{Mo_2O_7(H_2O)\}_2\{H_2Mo_2O_8(H_2O)\}$ $(H_2O)_{91}] \cdot 150H_2O$ ($\{Mo_{72}Fe_{30}\}_{cryst}$) into a nanostructure known as nanoblackberry ($\{Mo_{72}Fe_{30}\}_{NM}$) in aqueous solution (Fig. 3e).[96] This study not only successfully isolated the molybdenum nanoblackberries but also synthesized a tungsten analogue of the nanoblackberry, $Fe_3[W_{72}Fe_{30}O_{252}(CH_3COO)_2(-OH)_{25}(H_2O)_{103}] \cdot 180H_2O$ ($\{W_{72}Fe_{33}\}_{NM}$), using low-cost chemicals such as sodium tungstate, iron chloride and acetic acid solution. Both nanostructures exhibited potential as electrocatalysts for HER. It is worth noting that the structure of $\{W_{72}Fe_{33}\}_{NM}$ was more stable due to its stronger electronegativity. Furthermore, $\{W_{72}Fe_{33}\}_{NM}$ contained a large number of metal centers in their highest oxidation states, allowing the delocalization of electrons and accumulation of a significant number of protons, which resulted in an increased number of catalytic active sites. Importantly, the catalytic active sites were located on the central atomic Fe of the structural unit, rather than the coordinated Mo or W. These findings are significant for understanding the active centers of POM-assembled nanostructure catalysts and the development of efficient catalysts.

2.3.3 POM encapsulated metal–organic framework nanostructures. POM-encapsulated metal–organic framework (POM@MOF) nanostructures are hybrid materials that combine POMs with metal–organic frameworks (MOFs). In this case, POMs are encapsulated in the pores or channels of MOFs, resulting in a unique composite material with enhanced properties and functionalities.[97] The synthesis of POM@MOF nanostructures involves incorporating POMs during the MOF formation process, either through one-pot synthesis or post-synthetic encapsulation methods. The selection of POM and MOF components plays a crucial role in achieving successful encapsulation and desired properties. The encapsulation of POMs within MOFs offers several advantages. Firstly, it provides a protective environment for the POMs, preventing their aggregation and degradation. Secondly, the confinement within the MOF nanostructures can influence the properties and behaviors of the encapsulated POMs, such as their stability and catalytic activity. Additionally, the combination of POMs and MOFs can lead to synergistic effects and new functionalities that are not present in the individual components. POM@MOF nanostructures exhibit a well-ordered crystal or framework structures, enabling precise structural analysis of the catalysts. This presents new opportunities for the preparation of advanced materials in the field of electrocatalysis. Li *et al.* successfully synthesized a ZIF-67@POM hybrid material with a yolk/shell structure (Fig. 3f).[98] The shell of the ZIF-67@POM hybrid material was composed of ultrafine nanoparticles.

Moreover, through characterization techniques, it was revealed that the size of the ZIF-67@POM hybrid material was one order of magnitude smaller than that of the pristine materials. Due to the unique yolk/shell structure acting as a conductive medium to accelerate the charge transfer and prevent the accumulation of ZIF-67, as well as the synergistic effect of the high surface area and selective adsorption properties of the porous POM combined with the porosity of ZIF-67, the yolk/shell ZIF-67@POM hybrid material exhibited a high specific surface area, long-term stability and excellent electrocatalytic activity. The electrocatalytic performance can be significantly enhanced using a clearly defined molecular structure and designed morphology in nano-structured POM@MOF. Therefore, exploring new conjugated/amorphous/porous MOFs to support POMs holds great promise as a future direction.

3. POM-based single-crystal structures for electrocatalysis

Currently, the energy crisis continues to impact the development of countries worldwide. Therefore, it is urgent to replace disposable and environmentally harmful energy sources with eco-friendly, clean, and green energy.[99] To achieve this primary goal, the fundamental concept is to efficiently produce sustainable and clean energy (H_2) and convert greenhouse gases (CO_2) into energy and chemicals. Consequently, the conversion of effective energy sources has attracted significant attention, such as water splitting (HER and OER), as well as CO_2RR for converting greenhouse gases into chemicals. POM-based single-crystal structures have emerged as highly promising catalysts for a wide range of electrocatalytic reactions, which offer distinct advantages, including well-defined geometries, exceptional stability, adjustable redox properties and efficient electron and proton transfer capabilities. In this section, we summarize the applications of POM-based single-crystal structures in the field of electrocatalysis and provide detailed reports on the influence of different types of POMs on electrocatalytic performance, highlighting their potential in the fields of electrocatalysis and energy generation.

3.1 Hydrogen evolution reaction

POM-based single-crystal structures can be utilized to create superior active electrocatalysts and modulate their electrocatalytic properties. For instance, (I) POM-based single-crystal structures exhibit enhanced catalytic activity for HER due to their unique atomic arrangement and surface properties. This enables efficient electron transfer and promotes the adsorption and activation of hydrogen molecules, enhancing the HER activity.[72] (II) POM-based single-crystal structures enable a detailed understanding of the potential reaction mechanisms in HER. By utilizing advanced characterization techniques to explore active sites and reaction intermediates, complex electrocatalytic processes can be elucidated.[101] It provides valuable insights for the design and development of more efficient HER electrocatalysts.

This journal is © The Royal Society of Chemistry 2024

J. Mater. Chem. A, 2024, **12**, 13576–13604 | **13583**

3.1.1 Anderson-type POM-based single-crystal structures. In 2021, Singh and Das successfully synthesized a novel hybrid compound based on a POM, namely $[Cu^{II}(2,2'\text{-bpy})(H_2O)_2Cl]$ $[Cu^{II}(2,2'\text{-bpy})(H_2O)_2Al(OH)_6Mo_6O_{18}]\cdot 4H_2O$, which exhibited a unique helical chain structure.[100] This compound demonstrated remarkable electrocatalytic properties, specifically as an active catalyst for HER under neutral conditions. During the HER process, the Cl^- ion in the cationic segment of the compound was substituted by H_2O, resulting in a structural rearrangement and the generation of $\{Cu^{II}(2,2'\text{-bpy})(H_2O)_3\}^{2+}$. As a result, the interaction between this fragment and the Anderson-type POM was weakened, leading to the formation of a more stable complex, $K[Cu^{II}(2,2'\text{-bpy})(H_2O)_2Al(OH)_6Mo_6O_{18}]\cdot 4H_2O$. The derived catalyst exhibited an impressive current density (j) of 1 mA cm^{-2} at an overpotential of 348 mV in PBS buffer solution. Moreover, to gain insights into the role of POM, a comparative investigation was carried out using $[La(H_2O)_7\text{-}Al(OH)_6Mo_6O_{18}]_n\cdot 4nH_2O$ as an Anderson-type POM. Interestingly, the stand-alone Anderson-type POM demonstrated no catalytic activity, emphasizing the synergistic effect between the Cu-based complex and the POM.

3.1.2 Dawson-type POM-based single-crystal structures. Due to the inadequate adsorption or weak affinity for H in acidic conditions, transition metal complexes often exhibit suboptimal performances as electrocatalysts in HER. Consequently, developing highly efficient electrocatalysts for HER under acidic conditions has proven to be a challenging endeavor. Li et al. proposed a novel strategy to enhance the HER performance by incorporating POM-modified Ag materials, which effectively reduced the overpotential required for the reaction under acidic conditions.[101] The researchers synthesized an inorganic–organic hybrid compound by combining the $[P_2W_{18}O_{62}]^{6-}$ (P_2W_{18}) POM with Ag-2,2'-bipyrimidine (H_2biim), resulting in the formation of $\{K_2[(Ag_2(H_2biim)_2)_2(P_2W_{18}O_{62})]\cdot 2H_2O\}_n$. During the HER process, a reconstructive phenomenon occurred, leading to the in situ formation of Ag nanoparticles, while maintaining the fundamental structure of P_2W_{18}. The high conductivity of Ag nanoparticles was coupled with the excellent electron–proton storage capacity of POM, contributing to the enhanced HER performance. Moreover, the presence of POM ensured the more uniform dispersion of Ag nanoparticles throughout the catalyst. The resulting electrocatalyst exhibited exceptional activity and long-term stability, requiring an overpotential of only 91 mV at $j = 10$ mA cm^{-2}. Consequently, the introduction of POM offers a promising solution to address the insufficient H capture exhibited by transition metal complexes, thereby conferring superior HER performance.

Dawson-type POMs can be combined with transition metal complexes to enhance their HER performance under alkaline conditions. For example, Tian et al. successfully synthesized a POM-based hybrid derivative, denoted as $(Hbipy)_2[Mn(bipy)_3]_2[As_2W_{18}O_{62}]$, through a one-step hydrothermal synthesis method.[72] This approach involved the integration of transition metal complexes into the nanostructure of arsenic tungstate. The resulting compound exhibited a well-defined 3D topological network with organized 1D channels, which

contributed to its exceptional performance in HER. In an alkaline solution of 1 M KOH, the compound demonstrated an overpotential of 105 mV at $j = 10$ mA cm^{-2}. Furthermore, its Tafel slope was measured to be 98.9 mV dec^{-1}, indicating its favorable catalytic kinetics.

3.1.3 Saturated Keggin-type POM-based single-crystal structures. Saturated Keggin-type POMs are widely studied by researchers due to their large surface area and catalytically active terminal oxygen sites. Zhang et al. synthesized a novel 3D porous POM-based MOF by incorporating in situ-synthesized organic ligands and Co(II) ions.[102] The resulting compound, $Co_2(3,3'\text{-bpy})(3,5'\text{-bpp})(4,3'\text{-bpy})_3[SiW_{12}O_{40}]$ (4,3'-bpy = 4,3'-dipyridine, 3,5'-bpp = 3,5'-bis(pyrid-4-yl)pyridine, 3,3'-bpy = 3,3'-bis(pyrid-4-yl)dipyridine), featured two pairs of left- and right-handed double helices, which created triangular and rhombic channels (Fig. 4a). Remarkably, this compound exhibited excellent electrocatalytic activity for HER in a 1 M KOH aqueous solution, with a low overpotential of 92 mV and Tafel slope of 92.1 mV dec^{-1} at $j = 10$ mA cm^{-2} (Fig. 4b). These exceptional performance characteristics could be attributed to the synergistic effect between the W and Co elements and the presence of the highly negatively charged Keggin-type $[SiW_{12}O_{40}]^{4-}$ POM, which was encapsulated within the 3D porous framework and provided numerous active sites for the absorption of the intermediates (Fig. 4c). Supramolecular structures of crown ether-POM were explored by Shi et al., who successfully synthesized a supramolecular structure of crown ether-POM using the Keggin-type $[PW_{12}O_{40}]^{3-}$ POM as building blocks.[103] The $[Na(H_{24}C_{12}O_6)(CH_3CN)(H_2O)]_2[Na(H_{24}C_{12}O_6)(CH_3CN)_2]$ $[PW_{12}O_{40}]$ compound represented the first example of a supramolecular host–guest structure of a Keggin-type POM, where three [18]-crown-6 ether components were connected to the POM through hydrogen bonding and other intermolecular forces. In 0.5 M H_2SO_4 electrolyte, this compound exhibited an overpotential of 114 mV and Tafel slope of 229 mV dec^{-1} at $j = 10$ mA cm^{-2}.

3.1.4 Vacant Keggin-type POM-based single-crystal structures. Vacant Keggin-type POMs have attracted significant attention due to their unique properties and potential applications. These structures consist of Keggin-type POMs with one or more missing heteroatoms, leading to the presence of vacancies within the framework. The introduction of these vacancies can result in an enhanced electrocatalytic performance, making them promising candidates for application in the field of electrochemistry. In particular, $[BiW_9O_{33}]^{9-}$ (BiW_9) is very attractive. In 2022, Mulkapuri et al. successfully synthesized two compounds, $[\{H_3O\}_4\{Na_6(H_2O)_{22}\}][\{Cu^I(H_2O)_3\}_2\{Cu^{II}(H_2O)\}_3\{B\text{-}\alpha\text{-}Bi^{III}W_9^{VI}O_{33}\}_2]\cdot 7H_2O$ (NaCu-POM) and $Li_4[\{NH_4\}_2\{H_3O\}_3\{Li(H_2O)_5\}][\{Cu^{II}(SH)\}\{Cu^{II}Cu^I_{1.5}\}(B\text{-}\alpha\text{-}Bi^{III}W_9^{VI}O_{33})_2]\cdot 9H_2O$ (LiCu-POM), utilizing BiW_9 as building units.[104] These compounds consisted of mixed-valence copper wheel-functionalized structures sandwiched between two vacant Keggin anions of BiW_9, resulting in a bucket-like architecture (Fig. 4d). Interestingly, the catalytic active sites responsible for this electrocatalytic process were the W(VI) centers rather than the copper centers. The synergistic effect between the mixed-

13584 | J. Mater. Chem. A, 2024, 12, 13576–13604

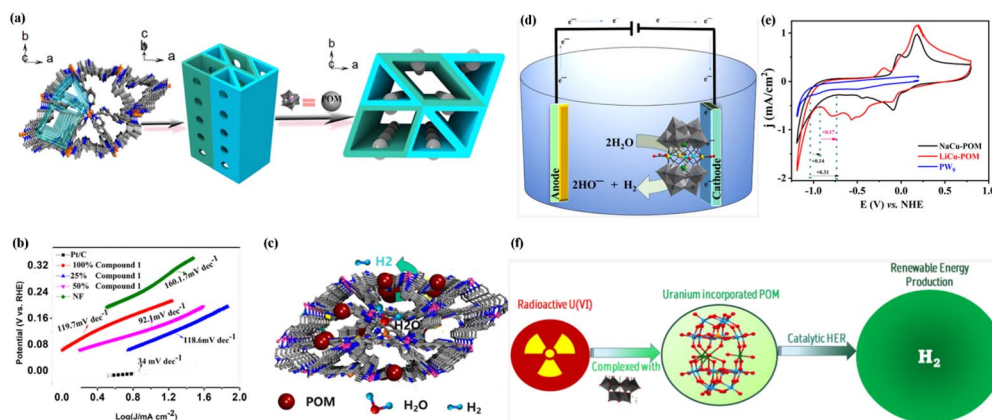This journal is © The Royal Society of Chemistry 2024

Fig. 4 (a) 3D POM-encapsulated MOF architecture. (b) Tafel plots of compound-doped composites with different contents. (c) Electrocatalytic schematic mechanism of compound for HER. Reproduced from ref. 102. Copyright 2022, the American Chemical Society. (d) Schematic diagram of water reduction involving the utilization of sandwich-type POM synthesized. (e) Cyclic voltammogram profiles for NaCu-POM, LiCu-POM and PW$_9$ were collected in 0.1 M potassium phosphate buffer used as an electrolyte. Reproduced from ref. 104. Copyright 2022, the American Chemical Society. (f) Schematic diagram of HER process involving the utilization of Finke-type POM synthesized with radioactive U(VI). Reproduced from ref. 106. Copyright 2023, the American Chemical Society.

valence wheel-shaped copper centers (Cu^{II}/Cu^{I}) and the tungsten centers (W^{6+}) enabled the entire system to efficiently catalyze the reduction of water to molecular hydrogen at neutral pH. NaCu-POM and LiCu-POM served as advanced HER catalysts, demonstrating overpotentials of 430 and 612 mV at $j = 1$ mA cm^{-2} (Fig. 4e), respectively. In the same year, Mulkapuri *et al.* successfully synthesized two compounds, Na$_6$[{Co^{II}(H$_2$O)$_3$}$_2${W^{VI}(OH)$_2$}$_2${Bi^{III}W$_9^{VI}$O$_{33}$}$_2$]·8H$_2$O and Na$_4$(Himi)$_2$[{Mn^{II}(H$_2$O)$_3$}$_2${W^{VI}(OH)$_2$}$_2${Bi^{III}W$_9^{VI}$O$_{33}$}$_2$]·28H$_2$O, which had W^{VI}-(OH)$_2$ functionalities attached to the surface of POM clusters.[105] Each compound possessed two *cis*-{W^{VI}(OH)$_2$} moieties as active sites for HER. These compounds exhibited remarkable electrocatalytic activity for the reduction of water to molecular hydrogen, with overpotentials of −726.04 mV and −643.52 mV at $j = 10$ mA cm^{-2} in a 0.1 M potassium phosphate electrolyte. The experimental results suggested that the presence of M^{n+}-OH groups/functionalities contributed to the electrochemical HER activity. These findings highlight the potential of POM-based catalysts with hierarchical active sites (M^{n+}-OH) and molecular control for sustainable clean energy generation.

3.1.5 Finke-type POM-based single-crystal structures. According to our understanding, radioactive nuclear waste is indeed a potential hazard, in addition to the harmful effects of toxic gases and emissions on human health and environmental protection. However, converting radioactive nuclear waste into electrocatalysts is a significant challenge. Through relentless efforts, an environmentally friendly electrocatalyst combining Finke-type POMs with radioactive nuclear waste was reported. Mulkapuri *et al.* first reported a sandwich-like Finke-type POM compound doped with radioactive nuclear waste ({UO$_2$}$^{2+}$), named K$_{10}$[{K$_4$(H$_2$O)$_6$}{UO$_2$}$_2$(α-PW$_9$O$_{34}$)$_2$]·13H$_2$O, which exhibited effective HER activity through water reduction (Fig. 4f).[106] Under the condition of a potassium chloride aqueous solution (0.1 M) as the supporting electrolyte, this compound showed overpotentials of 849.57 mV (at pH = 7) and

522.5 mV (at acidic pH = 3) at $j = 1$ mA cm^{-2}. Interestingly, the detailed electrochemical analysis revealed that the HER activity mediated by this compound is associated with the U^{VI}/U^{V} redox couple of the POM. This work holds great significance in the development of inexpensive and environmentally friendly POM-based electrocatalysts for achieving sustainable energy production.

3.1.6 Summary. The research on POM-based single-crystal structures in recent years has been limited, as indicated in Table 1. Most of the studies primarily focused on W-based POMs. Notably, Keggin and Dawson-type POMs played a crucial role in enhancing the HER performance. Among the W-based POMs, P$_2$W$_{18}$ stands out due to its low overpotentials, Tafel slopes and excellent stability over 1000 cycles. We performed a detailed analysis based on the study conducted by Li *et al.* on Keggin-type POMs and Dawson-type POMs.[101] In the electrocatalytic HER process, Dawson-type POMs generally exhibit superior performance compared to Keggin-type POMs, which can be attributed to the following factors: (I) structural and active sites differences: Dawson-type POMs and Keggin-type POMs possess distinct structures and active sites. (II) Electron transfer capability: Dawson-type POMs typically exhibit better electron transfer characteristics, which facilitate fast electron transfer and participation in catalytic reactions. In comparison, the electron transfer capability of Keggin-type POMs is relatively weaker. (III) Structural stability: Dawson-type POMs possess a stable framework structure, exhibiting good stability during catalytic reactions. Therefore, Dawson-type POMs can typically maintain catalytic activity for a longer period, thus demonstrating a better HER performance. However, there are few references on single-crystal structures of other types of POMs for HER applications. Furthermore, promising results have been obtained with POM-based nanostructures. In summary, Dawson-type POMs (P$_2$W$_{18}$) currently appear to be the optimal choice for obtaining POM-based single-crystal structures.

This journal is © The Royal Society of Chemistry 2024

J. Mater. Chem. A, 2024, **12**, 13576–13604 | **13585**

Table 1 Comparison of the HER performances of the POM-based electrocatalysts presented in this review

Type of POM	Electrocatalyst	Electrolyte	Overpotential (mV) @10 mA cm^{-2}	Tafel slope (mV dec^{-1})	Durability	Ref.
POM-based single-crystal structures						
Keggin	[Co-(phen)$_3$]$_2$[AsW$_{12}$O$_{40}$]·2H$_2$O	1 M KOH	121	134.1		74
	{[(Ag$_2$(H$_2$biim)(H$_2$biimCOO))$_2$H$_2$(SiW$_{12}$O$_{40}$)]·4H$_2$O}$_n$	0.5 M H$_2$SO$_4$	112	77	1000 cycles, 10 h	101
	[Na(H$_{24}$C$_{12}$O$_6$)(CH$_3$CN)(H$_2$O)]$_2$[Na(H$_{24}$C$_{12}$O$_6$)(CH$_3$CN)$_2$][PW$_{12}$O$_{40}$]	0.5 M H$_2$SO$_4$	114	229	10 h	103
	Co$_2${3,3'-bpy}[3,5'-bpp](4,3'-bpy)$_3$[SiW$_{12}$O$_{40}$]	1 M KOH	92	92.1	48 h	102
	(H$_2$bib)$_5$[Co$_4$(H$_2$O)$_2$(AsW$_9$O$_{34}$)$_2$]·2H$_2$O	1 M KOH	78	78.9	1000 cycles, 24 h	74
	Na$_6$[Co^{II}(H$_2$O)$_3$]$_2${W^{VI}(OH)$_2$}$_2${Bi^{III}W$_9$^{VI}O$_{33}$}$_2$]·8H$_2$O	0.1 M K$_3$PO$_4$	−726.04	173.8	1000 cycles, 10 h	105
	Na$_4$(Himi)$_2$[{Mn^{II}(H$_2$O)$_3$}$_2${W^{VI}(OH)}$_2$}$_2${Bi^{III}W$_9$^{VI}O$_{33}$}$_2$]·28H$_2$O	0.1 M K$_3$PO$_4$	−643.52	152.1	1000 cycles, 10 h	105
Dawson	(Hbipy)$_2$[Mn(bipy)$_3$]$_2$[As$_2$W$_{18}$O$_{62}$]	1 M KOH	105	98.9		74
	{K$_2$[(Ag$_2$(H$_2$biim)$_2$)$_2$(P$_2$W$_{18}$O$_{62}$)]·2H$_2$O}$_n$	0.5 M H$_2$SO$_4$	91	65	1000 cycles, 10 h	101
POM-based nanostructures						
Anderson	Cu/Mo$_2$C (CuMo$_6$)	1 M KOH	24	51.3	150 h	123
	Ni-MoB$_2$ (NiMo$_6$)	1 M KOH	65.4	58.3	200 h	124
	Co-MoB$_2$ (CoMo$_6$)	1 M KOH	91.3	76		124
	Fe-MoB$_2$ (FeMo$_6$)	1 M KOH	131	82.7		124
Evans–Showell	1T-Co-MoS$_2$@HMCS (Co$_2$MO$_{10}$)	1 M KOH	74	81	20 000 cycles, 40 h	134
		0.5 M H$_2$SO$_4$	132	78	20 000 cycles, 40 h	134
	CoS$_2$–MoS$_2$ (Co$_2$MO$_{10}$)	1 M KOH	120	64	3000 cycles, 24 h	135
		0.5 M H$_2$SO$_4$	153	71	3000 cycles, 24 h	135
Keggin	CoS$_2$@MoS$_2$@CC-30 h (GeMo$_{12}$)	1 M KOH	87	87	1000 cycles, 20 h	125
		0.5 M H$_2$SO$_4$	65	122	1000 cycles, 20 h	125
	MoS$_2$–Cu$_2$S-CC-24 h (PMo$_{12}$)	1 M KOH	159	109	1000 cycles, 24 h	127
	Cu$_2$S-MoS$_2$@CC-1 (PMo$_{12}$)	0.5 M H$_2$SO$_4$	150	61	1000 cycles, 94 h	128
	RuW/g-C$_3$N$_4$ (PW$_{11}$Ru)	0.5 M H$_2$SO$_4$	266	63	500 cycles	130
Isopolyoxomolybdates	Mo$_8$O$_{26}$-NbN$_x$O$_y$/NG (Mo$_8$)	1 M KOH	32	47	50 000 cycles	131
		0.5 M H$_2$SO$_4$	27	33	50 000 cycles	131
	[(TBA)Mo$_{12}$(AleThio)$_4$] (Mo$_{12}$)	0.5 M H$_2$SO$_4$	−77	80	2000 cycles	133

13586 | *J. Mater. Chem. A*, 2024, **12**, 13576–13604

This journal is © The Royal Society of Chemistry 2024

3.2 Oxygen evolution reaction

The design and synthesis of efficient OER catalysts are crucial for improving the energy efficiency of water splitting.[107] POM-based compounds have been explored as effective homogeneous/heterogeneous electrocatalysts for OER due to their rich redox chemistry. In particular, the combination of different transition metals in POM-based single-crystal structures can enhance the catalytic activity of POMs. This is because the different oxidation states and coordination geometries of transition metals influence the OER mechanism and their different degrees of activation in the electrolyte.[110]

3.2.1 Dawson-type POM-based single-crystal structures. Unique open structures expose more active sites, thereby enhancing the electrocatalytic activity. Thus, the open structure of Dawson-type POMs has been extensively investigated due to their ability to undergo substitution with transition metals and related functional groups. Li et al. synthesized two new cobalt-substituted Dawson-type POMs, $K_7H_2[K(Co(H_2O)_4)_2$-$Co(H_2O)_2(Si_2W_{18}O_{66})]\cdot 22H_2O$ and $K_7H_2[\{C(NH_2)_3\}(Co(H_2O)_4)_2Co(H_2O)_2(Si_2W_{18}O_{66})]$ (K-$Co_3Si_2W_{18}$

and C(NH_2)_3–$Co_3Si_2W_{18}$), which exhibited different pore angles due to the incorporation of different templates.[107] The introduction of various types, positions, and quantities of templating ions led to changes in the structural angles of these POMs. Both compounds demonstrated excellent OER activity, with K-$Co_3Si_2W_{18}$ achieving a catalytic current of 395.11 A in a neutral PBS solution. The catalytically active center (CoO_x) was generated as an intermediate through the decomposition of the Dawson-type POM.

The assembly of large-ring POMs with $[Pt(H_2O)_2(OH)_4]$ moieties has been a topic of great interest in promoting electrocatalytic capabilities. Kuznetsova et al. successfully synthesized $K_{22}(NH_4)_9H_3[\{Pt(OH)_3(H_2O)\}_6P_8W_{48}O_{184}]\cdot 79H_2O$ by combining the large-ring inorganic Dawson-type POM cavity $Li_{17}(NH_4)_{21}H_2[P_8W_{48}O_{184}]$ with $[Pt(H_2O)_2(OH)_4]$.[108] Remarkably, this compound possessed an enormous surface area with up to six $\{Pt(H_2O)_x(OH)_{4-x}\}$ building blocks coordinated within the Dawson-type POM, making it the largest Pt-enriched POM structure reported to date. Extensive electrochemical studies demonstrated its electrocatalytic activity for water oxidation, both in solution and as an electrode. Furthermore, comparing

Fig. 5 (a) Polyhedral representation of Co_4-WS and Fe_4-WS. (b) Water oxidation mechanism using Fe-POMs considered as single-site catalysts. Potentials and energies correspond to the catalytic cycle computed for the Fe_4-WS electrocatalyst. The dark green square indicates the active species. Reproduced from ref. 110. Copyright 2022, The Royal Chemistry Society. (c) Scheme showing the assembly process of POV-based hybrid compounds **1–3**. (d) Scheme showing the structural conversion of compound **1** during OER. Reproduced from ref. 111. Copyright 2020, Elsevier B.V. All rights reserved.

This journal is © The Royal Society of Chemistry 2024

J. Mater. Chem. A, 2024, 12, 13576–13604 | **13587**

the cyclic voltammetry (CV) of the system with and without POM, it was concluded that the successful introduction of POM promoted the reduction of Pt(IV) to Pt(II) and its subsequent re-oxidation to Pt(IV). This finding opens up new avenues for exploring the electrocatalytic effects of introducing Pt-based moieties into large-ring POMs in aqueous solution.

3.2.2 Saturated Keggin-type POM-based single-crystal structures. In 2022, Sood et al. successfully synthesized a rare Keggin-type POM cluster, namely $(C_5H_7N_2)_6[NiW_{12}O_{44}]$ (PS-78).[109] It was intriguing that this distinct cluster displays a Silverton-like structure, featuring a central Ni atom coordinated in an octahedral environment, while also preserving other structural characteristics typical of the Keggin-type POM. PS-78 emerged as a promising catalyst for OER in alkaline electrolyte, exhibiting remarkable efficiency and long-term stability. PS-78 had an overpotential of only 347 mV at $j = 10$ mA cm^{-2} and remained stable for up to 96 h. Mechanistic investigations unveiled that the in situ formation of NiO and WO$_x$ ($x = 1, 2$) species plays a crucial role as the active intermediates in the OER process.

3.2.3 Finke-type POM-based single-crystal structures. Co-POM has gained significant recognition as a highly influential catalyst for water oxidation due to its metal oxide fragments and distinct discrete structure of POM. However, besides Co, Fe possesses strong redox capabilities owing to its diverse oxidation states. Thus, to investigate the activity relationship between Co and Fe with POM and explore their electronic activity, Azmani et al. synthesized $[(Fe^{III}OH_2)_2Fe_2^{III}(B-a-PW_9O_{34})_2]^{6-}$ (Fe$_4$-WS) and $[(Fe^{III}OH_2)PW_{11}O_{39}]^{4-}$ (Fe–K) Finke-type POMs and assessed their electrocatalytic OER activity in a neutral medium, comparing them with the tetra-cobalt Weakley sandwich $[Co_4^{II}(H_2O)_2(B-a-PW_9O_{34})_2]^{10-}$ (Co$_4$-WS) (Fig. 5a).[110] OER experiments were performed using a barium salt-modified carbon paste electrode, and the computational results indicated that both Fe-POMs exhibited similar OER activity, albeit with slightly slower kinetics compared to their Co-POM counterpart. Despite the apparent electronic differences between Fe$_4$-WS and Co$_4$-WS, they demonstrated similar reaction mechanisms, primarily involving two steps, as follows: (i) the potential-limiting step caused by proton-coupled electron transfer (PCET) (from Fe^{III}–OH to Fe^{IV}=O) and (ii) a chemically limiting step corresponding to O–O bond formation during a water nucleophilic attack (WNA), with an associated activation barrier of 0.86 eV (Fig. 5b). The latter mechanism is similar to other proposed mechanisms for water oxidation, where typically two protons and two electrons are released before WNA. The difference lies in the fact that the S$_0$ (Fe^{II}–OH$_2$) species undergoes natural PCET events in solution under aerobic conditions, while S$_1$ (Fe^{III}–OH) species are produced in crystalline solids. Notably, hydrogen bonding also played a role in the reaction, contributing to a reduction in the activation barrier for O–O bond formation. The lower Tafel slope observed for Co$_4$-WS indicated faster kinetics compared to Fe$_4$-WS, which is consistent with the lower activation barrier observed for Co-POM. Interestingly, despite the significant differences in the electronic structures of Fe^{III}-POM and Co^{II}-POM, a similar overpotential was observed. Fe^{III}-POM proved to be stable under heterogeneous electrocatalytic conditions and

exhibited activity as an OER catalyst. Consequently, several conclusions can be inferred: the activity of POM is influenced by its nuclearity, with the Finke-type POM displaying slightly superior electrocatalytic activity compared to the Keggin-type POM. Additionally, the significant role of hydrogen bonding should not be overlooked. Finke-type POMs show stronger hydrogen bonding ability compared with Keggin-type POMs, which can greatly reduce the activation energy of the reaction.

3.2.4 Iso-POM-based single-crystal structures. Iso-POMs represent an important class of compounds within the broader category of POMs. Iso-POMs, including iso-polyoxovanadates and isopolyoxomolybdates, are widely recognized as representative examples of this unique class of compounds. Here, we examine the influence of these two iso-POM types on the performance of OER.

Isopolyoxovanadates. Hu et al. synthesized three inorganic–organic compounds based on isopolyoxovanadates, $[Ni_2(BBTZ)(H_2O)_4]V_4O_{12} \cdot 2H_2O$ (1), $[Co_2(BBTZ)(H_2O)_4]V_4O_{12} \cdot 2H_2O$ (2) and $[Ni(BBTZ)_2]V_2O_6 \cdot 2H_2O$ (3) (BBTZ = 1,4-bis-(1,2,4-triazole-1-ylmethylene)benzene), which were investigated for their OER performance in 1 M KOH electrolyte (Fig. 5c).[111] Compounds 1 and 2 possessed a 2D layered structure, while compound 3 featured a 3D framework with a five-fold inter-penetrating metal–organic structure. During the OER process, structural transformations were observed in compounds 1–3. The organic BBTZ ligand and most of the isopolyoxovanadates species on the surface of compounds 1–3 were electrochemically separated at the anodic potential, dispersing them in the electrolyte and leaving V-doped transition metal hydroxide as the residual material. Importantly, the intermediate transition metal hydroxides formed during the OER process serve as the active centers for the electrocatalytic reaction, indicating that isopolyoxovanadate salts are not the active sites. Under alkaline electrocatalytic conditions for OER, this type of isopolyoxovanadate-based crystalline material undergoes a structural transformation process (Fig. 5d). Dissociation of the organic BBTZ ligand from the crystal lattice occurs, followed by the conversion of the original coordination network structure into a mixed intermediate comprised of NiOOH, NiV$_2$O$_6$, and V$_2$O$_5$. Kar et al. synthesized three compounds based on the coordination of the decavanadate anion ($[V_{10}O_{28}]^{6-}$) with transition metal ions, with the general formula $\{[(H_2O)_2K-\mu-(H_2O)_3M(H_2O)_3]_{2n}[V_{10}O_{28}]_n\}$ (M = Mn^{2+}, Co^{2+} and Ni^{2+}).[112] All these compounds, denoted as 1–3, were evaluated for their OER performance under alkaline conditions (0.1 M KOH). Similar to the previously mentioned compounds, these compounds exhibited structural instability during the OER process. Furthermore, it was observed that they produced V-doped metal hydroxides as the true active sites in alkaline media.

Isopolyoxomolybdates. The investigation of reaction mechanisms in giant POM clusters is often challenging due to their complex structures and oxidation states. However, in the groundbreaking study by Li et al. in 2023, they utilized an operando Raman system with flowing water to visualize the reaction process of isopolyoxomolybdates during the OER process.[113] This innovative approach enabled the determination of the crystal structures of the clusters during the OER process,

13588 | J. Mater. Chem. A, 2024, **12**, 13576–13604

This journal is © The Royal Society of Chemistry 2024

providing valuable insights into the intermediate active sites in cluster electrocatalysis. Starting with Na_2MoO_4 as the precursor and using H_2SO_4 as the electrolyte, a sequential acidification process was employed to create $Mo_7O_{24}{}^{6-}$ ($\{Mo_7\}$) and high-nuclearity $Mo_{36}O_{112}{}^{8-}$ ($\{Mo_{36}\}$) clusters. The final polymerization product was identified as $[H_6K_2Mo_3O_{12}(SO_4)]_n$ ($\{Mo_3(SO_4)\}_n$). To precisely control the electrochemical synthesis of Mo-based compounds and generate molybdenum clusters with mixed oxidation states, a water-based flow-electrochemical synthesis cell was developed. The experimental evidence revealed that only $\{Mo_{36}\}$ and $\{Mo_3(SO_4)\}_n$ clusters were capable of transforming into the larger clusters $\{Mo_{154}\}$ and $\{Mo_{102}\}$ during the OER process. Furthermore, this study highlighted the crucial role of H^+/e^- under acidic conditions in the reduction of intermediate clusters. Acidic decomposition of $\{Mo_{36}\}$ and $\{Mo_5(SO_4)\}$ clusters resulted in the formation of $\{Mo_5\}$ and $\{Mo_3(SO_4)\}_n$ monomers, which further self-assembled into the larger clusters $\{Mo_{154}\}$ and $\{Mo_{102}\}$ under the electrocatalytic conditions.

In parallel research, Zeng et al. compared the OER capabilities of conventional POMs with transition metal-incorporated derivatives.[114] Three functional framework compounds, $\{CoO_6\text{-}Mo_8O_{28}\}_n$ (**1**), $\{\gamma\text{-}Mo_8O_{26}\}_n$ (**2**) and $\{\alpha\text{-}Mo_8O_{26}\}$ (**3**), were synthesized using the conventional solution method. Compound **1** possessed a pure 2D inorganic $\{CoO_6Mo_8O_{28}\}_n$ framework,

compound **2** had a 1D structure, and compound **3** exhibited a 0D structure. Compared to the traditional $\{Mo_8O_{26}\}$ clusters, the 2D porous $\{CoO_6Mo_8O_{28}\}_n$ catalyst exhibited a lower over-potential (293 mV at $j = 10$ mA cm^{-2}) and smaller Tafel slope (53 mV dec^{-1}) for water oxidation. The high-resolution XPS analysis indicated a synergistic effect between Co2p and Mo3d during the water oxidation process, highlighting the enhanced OER performance achieved through the synergistic doping of transition metal elements in conventional POMs.

3.2.5 Summary. In the field of POM-based single-crystal structures, it is obvious that both isopolyvanadates and iso-polymolybdates exhibit low overpotentials and Tafel slopes (Table 2). According to our analysis, the reason why iso-polyoxovanadates and isopolyoxomolybdates show superior electrocatalytic OER performances compared with iso-polyoxotungstates can be attributed to the fact that the d-electron orbital energy levels of Mo and V in iso-polyoxomolybdates and isopolyoxovanadates are more suitable for catalytic OER. In contrast, the d-electron orbital energy level of W is relatively higher.[109,111] Simultaneously, the introduction of transition metals in POM-based electrocatalysts can also stabilize catalytically active intermediates, thereby enhancing the selectivity and yield of the OER. In contrast, the influence of tungsten ions in isopolyoxotungstates on the intermediate stability is relatively weaker.[111,114] Alternatively, transition metal

Table 2 Comparison of the OER performance of the POM-based electrocatalysts presented in this review

Type of POM	Electrocatalyst	Electrolyte	Overpotential (mV)@10 mA cm^{-2}	Tafel slope (mV dec^{-1})	Durability	Ref.
POM-based single-crystal structures						
Keggin isopolyoxovanadates	$(C_5H_7N_2)_6[NiW_{12}O_{44}]$	1 M KOH	347	130	96 h	109
	$[Ni_2(BBTZ)(H_2O)_4]V_4O_{12}\cdot2H_2O$	1 M KOH	353	77.8	12 h	111
	$[Co_2(BBTZ)(H_2O)_4]V_4O_{12}\cdot2H_2O$	1 M KOH	395	88.9	12 h	111
	$[Ni(BBTZ)_2]V_2O_6\cdot2H_2O$	1 M KOH	433	81.8	12 h	111
	$\{[[(H_2O)_2K\text{-}\mu\text{-}(H_2O)_3Mn(H_2O)_3]_{2n}[V_{10}O_{28}]_n\}$	0.1 M KOH	290	122		112
	$\{[[(H_2O)_2K\text{-}\mu\text{-}(H_2O)_3Co(H_2O)_3]_{2n}[V_{10}O_{28}]_n\}$	0.1 M KOH	300	119		112
	$\{[[(H_2O)_2K\text{-}\mu\text{-}(H_2O)_3Ni(H_2O)_3]_{2n}[V_{10}O_{28}]_n\}$	0.1 M KOH	270	89	8 h	112
Isopolyoxomolybdates	$\{CoO_6Mo_8O_{28}\}_n$	1 M KOH	293	53	24 h	114
	$\{\gamma\text{-}Mo_8O_{26}\}_n$	1 M KOH	303	59		114
	$\{\alpha\text{-}Mo_8O_{26}\}$	1 M KOH	316	64		114
POM-based nanostructures						
Anderson	AB&PS-13 (AlMo$_6$)	1 M KOH	330	90	40 h	136
	Fe-S-NiMoO$_4$/MoO$_3$@NF (FeMo$_6$)	0.1 M KOH	490	60	10 h	149
Finke	$Co_4(PW_9)_2$@Co@C	0.1 M KOH	430	120		150
	$Co_4(PW_9)_2$@Co/Ni@C	0.1 M KOH	400	67	12 h	150
	$Co_4(PW_9)_2$@N, S-Co@C	0.1 M KOH	410	62	12 h	150
	$Co_4(PW_9)_2$@N,S-Co/Ni@C	0.1 M KOH	460	88		150
Keggin	NiFe-LDH-PW$_{12}$-X-12 h	1 M KOH	291	78.3	40 h	138
	PW$_{12}$/Ag/graphene-a	0.1 M PBS	540	190		139
	PW$_{12}$/Ag/graphene-b	0.1 M PBS	610	192		139
	$\{Cu_2SiW_{12}O_{40}\}$@HKUST-1	1 M KOH	340	73	25 h	140
	PW$_{12}$@amZIFs	1 M KOH	306	54	14 h	141
	SiW$_9$Co$_3$@ZIF-8	0.1 M KOH	2730	69.4		143
	SiW$_9$Co$_3$@ZIF-67	0.1 M KOH	470	113.6	12 h	144
	SiW$_9$Co$_3$[h]@ZIF-67	0.1 M KOH	420	93.9	12 h	144
	PW$_6$Mo$_6$/ZIF-67@NF	1 M KOH	201	55	24 h	146
	GeW$_9$@NiF	1 M KOH	370	84	8 h	147
		PBS (pH = 14)	530	153	8 h	147

This journal is © The Royal Society of Chemistry 2024

J. Mater. Chem. A, 2024, **12**, 13576–13604 | **13589**

ion doping can adjust the stability of the reaction intermediates, reducing their dissociation and competing reactions.[112,114] In conclusion, stable structures containing molybdenum and vanadium as heteropolyanions are the optimal choice for OER.

3.3 CO_2 reduction

The target of CO_2RR is to obtain products through proton-coupled multi-electron transfer mechanisms, typically categorized as C1 and C$n \geq$ 2 reduction products.[115] However, the competitive HER often occurs during the electrocatalytic CO_2 reduction process, greatly reducing the conversion efficiency of CO_2. Therefore, for the development of CO_2RR, it is very important to find efficient electrocatalysts that can inhibit HER. In this case, POMs can promote the formation of hydrogen bond networks near the CO_2 coordination center, facilitating proton-coupled electron transfer when the proton source approaches the catalytic active center.[116] Specifically, transition metal-substituted POMs may form reversible complexes with CO_2 fixation or reaction, which appears favorable for electrocatalytic CO_2RR, and can serve as attractive homogeneous or heterogeneous electrocatalysts.[63]

3.3.1 Saturated Keggin-type POM-based single-crystal structures. Huang *et al.* conducted a study in which they synthesized a series of metal–organic frameworks (M-POMOFs) by assembling Keggin-type POMs and hexatopic M-TCPP linkers (Fig. 6a).[115] Their study aimed to uncover the underlying reaction principles between POMs and metal centers during the CO_2RR process. Among the synthesized M-POMOFs, Fe-POMOF demonstrated exceptional selectivity in electrochemically converting CO_2 into CO, achieving an impressive FE of 92.1%. Throughout the catalytic process, the Fe-TCPP center played a crucial role as the active center in the catalyst, with electron transfer occurring from the POM to the Fe-TCPP. Additionally, it was observed that the oxidation state of Mo within POM remained unchanged following CO_2RR, suggesting that POM possessed the ability to capture electrons at an external reduction potential, and subsequently transfer them to the Fe-TCPP center, resulting in the generation of CO (Fig. 6b). We speculate that POM, which is known for its multi-electron characteristics, acted as an electron donor, while the electron-deficient structure of Fe-TCPP attracted electrons, thereby facilitating the establishment of an electronic pathway through which POM could supply electrons to the metal center. The synergistic interaction between POM and Fe-TCPP played a vital role in optimizing the CO_2RR process.

3.3.2 Isopolyoxomolybdate-based single-crystal structures. The generation of C_2 products in CO_2RR has emerged as a highly relevant research area within the field of electrocatalysis. The production efficiency of C_2 products can be significantly impacted by the modulation of single-crystal structures, leading to extensive investigations into single crystal architectures. In the study conducted in 2022 by Fang *et al.*, they employed a template-assisted strategy to synthesize seven high-nuclearity acetylide copper clusters.[116] These clusters, namely Cu_{36} and Cu_{56}, were formed through the assembly of $[M@(V/PO_4)_6]$ (M: Cu^{2+}, Na^+, K^+) framework sequences, resulting in a multi-nuclear structure. The electronic and physical properties of these clusters were found to be influenced by both the internal template and the external phosphine acid ligands. Additionally, the electrocatalytic performance of the clusters in CO_2RR was influenced by both their surface morphology and internal VO_4/PO_4 template. Notably, the internal PO_4 template and the external naphthyl groups exhibited a promoting effect on the generation of C_2 products (C_2H_4 and C_2H_5OH). This also highlights the significant role of templates in the field of electrocatalysis, providing valuable insights for future researchers to explore.

3.3.3 Summary. Given the scarcity of reports on POM-based single-crystal structures, we consolidated the nanostructures and single-crystal structures in Section 4.3, where further elaboration on this matter can be found.

4. POM-based nanostructures for electrocatalysis

POM-based nanostructures demonstrate tremendous potential as highly efficient catalysts for a wide range of electrocatalytic reactions. By reducing the size of POM-based materials from bulk solids to the nanoscale, these nanostructures exhibit a significantly larger surface area and enhanced reaction activity.[117] As a result, POM-based nanostructures offer improved efficiency and expanded application possibilities in electrocatalysis and energy conversion. Additionally, the combination of nanostructures and POM leads to a synergistic effect, in which the assembly structure facilitates shorter diffusion paths and provides more accessible active sites.[118] The

Fig. 6 (a) Crystal structures of M-POMOFs. (b) Proposed reaction mechanism in PCR and ECR (photo- and electrocatalytic CO_2 reduction) reactions for Fe-POMOF, respectively. Reproduced from ref. 115. Copyright 2022, The Authors, some rights reserved; exclusive licensee American Association for the Advancement of Science.

13590 | *J. Mater. Chem. A*, 2024, **12**, 13576–13604

This journal is © The Royal Society of Chemistry 2024

synthesis and modification of POM-based nanostructures can be precisely tailored to achieve the desired performance and enhanced catalytic activity.[119] Strategies such as doping, surface functionalization and hybridization with other materials further enhance their electrocatalytic efficiency and stability. Overall, these exceptional characteristics position POM-based nanostructures as highly appealing candidates for electrocatalytic applications.

4.1 Hydrogen evolution reaction

Functionalizing POM-based electrocatalysts on different types of conductive materials through covalent or non-covalent interactions has become an important direction for achieving a superior HER performance.[120,121] With the synergistic effect of the combination of POMs with high redox ability and highly conductive materials, many advantages of POM-based nanostructures are revealed.[122] (I) Their unique nanoscale morphology provides a large surface area-to-volume ratio, increasing the number of exposed active sites for electrocatalytic reactions. This increased surface area facilitates a higher density of catalytic active sites, thereby improving the HER performance. (II) POM-based nanostructures typically exhibit excellent electron conductivity. This characteristic allows for efficient charge transfer during the HER process, reducing the energy losses and improving the overall catalytic efficiency. (III) POM-based nanostructures can be easily functionalized or modified to adjust their catalytic properties. By introducing specific functional groups or different metal ions, the catalytic activity and selectivity of POM-based nanomaterials can be finely tuned.

4.1.1 Anderson-type POM-based nanostructures. The water interface plays a crucial role in the synthesis of nanomaterials

Fig. 7 (a) Schematic illustration of the preparation of Cu/Mo$_2$C. (b) SEM images of the as-synthesized Cu/Mo$_2$C. Reproduced from ref. 123. Copyright 2023, Tsinghua University Press. (c) Schematic illustration of the guided synthesis of TM single atoms supported on MoB$_2$ (TM = Ni, Co, Fe) applying Anderson-type POMs as molecular precursor. (d) Left: crystal structure of Ni–MoB$_2$ with one Mo substituted by one Ni in a 2 × 2 × 2 supercell. Right: top view of the (100) facet cleaved from the crystal and the labeling of the possible reactive sites for intermediate adsorption. Reproduced from ref. 124. Copyright 2023, the American Chemical Society. (e) Strategy for the formation of CoS$_2$@MoS$_2$@CC. (f) Overpotentials of CoS$_2$@MoS$_2$@CC–30 h and the reported MoS$_2$-based electrocatalysts for comparison at 10 mA cm^{-2} in 0.5 M H$_2$SO$_4$ and 1.0 M KOH electrolyte. Reproduced from ref. 125. Copyright 2020, Wiley-VCH GmbH. (g) Schematic illustration of Mo$_8$O$_{26}$-NbN$_x$O$_y$ heterostructure. (h) Charge density difference diagram of Mo$_8$O$_{26}$−Nb$_4$N$_5$. (i) Side view of schematic models for H$_2$O dissociation on Nb$_4$N$_5$ and Mo$_8$O$_{26}$−Nb$_4$N$_5$ surfaces. Reproduced from ref. 131. Copyright 2023, Wiley-VCH GmbH.

This journal is © The Royal Society of Chemistry 2024

J. Mater. Chem. A, 2024, **12**, 13576–13604 | **13591**

as electrocatalysts. Its high mobility makes the optimization of the water structure at the interface essential for improving the catalytic performance. In the study by Jin et al., they prepared Cu/Mo_2C composite catalysts using an Anderson-type POM ($CuMo_6$) as a precursor and carefully adjusted the $CuMo_6$ structure to enhance the performance of the electrocatalyst (Fig. 7a).[123] The composite material was composed of layered structures comprised of smaller particles that adhered to the surface of NF, forming a thin film with a stacked layered pattern (Fig. 7b). The positively charged Cu species activated water molecules and modulated the charge distribution in the d-band center of Mo_2C, leading to an optimized water interface structure and reduced H adsorption. This optimization facilitated the movement of the reaction intermediates through the water layer at the interface, thereby enhancing the HER performance. The optimized Cu/Mo_2C catalyst demonstrated overpotentials of 24 and 178 mV at $j = 10$ and 1000 mA cm^{-2}, respectively.

The development of single-atom catalysts (SACs) and the exploration of the interactions between individual atoms and supports are crucial for identifying the active sites and elucidating catalytic mechanisms. Yang et al. utilized Anderson-type POMs ($NiMo_6$, $CoMo_6$ and $FeMo_6$) as precursors and loaded a series of transition metals (TM = Ni, Co, Fe) onto MoB_2 (TM-MoB_2), achieving a remarkably high loading of TM (6.72–7.03 wt%) (Fig. 7c).[124] The TM modification significantly enhanced the HER activity of MoB_2, with Ni–MoB_2 demonstrating the optimal performance in both alkaline and acidic solutions. DFT calculations demonstrated the significance of different surfaces, namely the NiMo-terminated and B-terminated (100) facets, when splitting the bulk Ni–MoB_2 structure along the (100) plane (Fig. 7d). The (100) surface terminated with NiMo atoms is much more stable in terms of energy (6.29 eV) compared to the B-terminated (100) surface. It was revealed that the true active site is a MoB_2-based SAC. The introduction of transition metals reduced the hydrolysis barrier of Mo in the system and enhanced its H adsorption capability, confirming that the Mo provided by the POM serves as the genuine chemical adsorption site. Interestingly, the introduction of TMs can enhance the HER activity, which can be attributed to the modulation of the different electronic states between the positively charged Ni and negatively charged material surface, thereby facilitating the adsorption of H by the electrocatalyst.

4.1.2 Saturated Keggin-type POM-based nanostructures.

The utilization of highly crystalline POM-based compounds as precursors for the synthesis of nanomaterials offers exceptional stability, enabling the resulting nanomaterials to withstand a wide range of pH values and expanding their application potential as electrocatalysts. This approach has attracted considerable attention from researchers but is recognized as a challenging endeavor. In the study by Hou et al., they employed a novel precursor, $\{L_3Co_2 \cdot 6H_2O\}[H_3GeMo_{12}O_{40}] \cdot 9H_2O$ (L = 1,2,4-triazole), catalyzed by thiourea (TU) to fabricate a $CoS_2@MoS_2@CC$ nanocomposite array on carbon cloth (CC) (Fig. 7e).[125] The $CoS_2@MoS_2@CC$-30 h composite material exhibited excellent activity and stability for HER in both acidic and alkaline media. It achieved a low overpotential of 65 mV in

0.5 M H_2SO_4 and 87 mV in 1.0 M KOH, which were much lower than that of other materials at $j = 10$ mA cm^{-2} (Fig. 7f). Li et al. synthesized a novel 2D MoCu-POMOF, $[Cu(4-pyz)]_4@(PMo_{12}O_{40})$ (4-pyz = 4-(pyridin-4-yl) benzoic acid), through a simple hydrothermal method, encapsulating PMo_{12} within the cavities of a 2D Cu-MOF.[126] The oxygen-rich PMo_{12} provided abundant sources of molybdenum and oxidation capability for the MoO_2 nanomaterials. The $MoO_2/MoOC$ nanomaterials with embedded Pt nanoparticles were obtained by high-temperature calcination, which exposed more porous structures and increased the electrochemically active surface area. The strong synergistic effect between the Pt nanoparticles as the active center and $MoO_2/MoOC$ with good electrochemical conductivity was responsible for the excellent HER activity of $Pt@MoO_2/MoOC$. Additionally, Che et al. synthesized a new POM-based metal–organic compound $[\{Cu(bipy)\}_6(Mo_6^{VI}O_{22})][PMo^VMo_{11}^{VI}O_{40}]$ as a precursor, which subsequently formed in situ molybdenum sulfide directly coupled to CC within 24 h, resulting in the formation of the MoS_2–Cu_2S-CC-24 h electrode with highly dispersed nanosheets.[127] This electrocatalyst demonstrated an outstanding performance for HER in 1.0 M KOH, exhibiting a low overpotential of 159 mV and a smaller Tafel slope of 109 mV dec^{-1}. Furthermore, the multi-interface engineering strategy has recently attracted significant attention due to its ability to enhance the conductivity of electrocatalysts and the adsorption capacity of the electrochemical intermediates. Jin et al. pioneered the synthesis of a POM-based copper metal–organic framework, $[\{Cu^{II}(C_{10}N_6H_7)_4(H_2O)_2\}H_6(PMo_{12}O_{40})_2] \cdot 12H_2O$ [$C_{10}N_6H_7$: 3-(1H-pyrazol-4-yl)-5-(pyridin-4-yl)-1,2,4-triazole], as a precursor. Then, they utilized the hydrothermal method with TU and CC to fabricate the Cu_2S-$MoS_2@CC$-1 nanocomposite.[128] In 0.5 M H_2SO_4, Cu_2S-$MoS_2@CC$-1 exhibited remarkable HER activity, which could be attributed to the synergistic effect between Cu_2S and MoS_2. Notably, Cu_2S-$MoS_2@CC$-1 achieved a low overpotential of 150 mV at $j = 10$ mA cm^{-2}, accompanied by a Tafel slope of 61 mV dec^{-1}.

The incorporation of highly conductive compounds on the surface of nanomaterials has shown great potential in enhancing their overall electrocatalytic activity and durability. Transition metal phosphides (TMP) and graphitic carbon nitride (g-C_3N_4) have emerged as promising candidates in this research area. In the study by Shi et al., polypyrrole, PMo_{12}, and Ni^{2+} were utilized as supramolecular precursors. Through electrostatic attraction and high-temperature calcination, carbon-coated porous nanospheres were successfully prepared as electrocatalysts ($MoP/MoNiP@C$).[129] The introduction of conductive materials during the calcination process significantly improved the conductivity of the transition metals, thereby further enhancing the performance of the catalysts in HER. The use of polypyrrole and Keggin-type POM not only served as a source of phosphorus and molybdenum, respectively, but also facilitated charge transfer, leading to increased efficiency. Another study conducted by Pathan et al. involved the synthesis of highly dispersed RuW/g-C_3N_4 composite materials.[130] This was achieved by complexing a ruthenium-substituted POM ($PW_{11}Ru$) with melamine, followed by

13592 | J. Mater. Chem. A, 2024, 12, 13576–13604

This journal is © The Royal Society of Chemistry 2024

calcination under an inert atmosphere. The RuW/g-C$_3$N$_4$ composite displayed improved electrochemical activity for HER, with an overpotential of approximately 266 mV at $j = 10$ mA cm^{-2} and a Tafel slope of 63 mV dec^{-1}.

4.1.3 Isopolyoxomolybdate-based nanostructures. The incorporation of POM materials on positively charged surfaces has been demonstrated to be advantageous for optimizing their HER performance. In the study by Yang *et al.*, they utilized a controllable hydrothermal nitridation process to load oxygen-rich Mo$_8$O$_{26}$ clusters onto NbN$_x$O$_y$/NG (NG = N-doped graphene) nanocomposites with an approximate size of 1.0 nm (Mo$_8$O$_{26}$-NbN$_x$O$_y$/NG) (Fig. 7g).[131] The uniform confinement of the Mo$_8$O$_{26}$-NbN$_x$O$_y$ heterocatalyst within the NbN$_x$O$_y$ nanodomains through shared O and N atoms resulted in the exposure of abundant active sites, leading to superior HER activity and stability in pH-neutral electrolyte. The charge density difference diagram revealed that the covalent bonds between the Mo$_8$O$_{26}$ cluster and the NbN$_x$O$_y$ nanodomains on the surface facilitated a unique interfacial configuration and favorable electronic structure. In the Mo$_8$O$_{26}$-Nb$_4$N$_5$ heterostructure connected by Mo-(O,N)-Nb motifs, Nb$_4$N$_5$ transfers a Bader charge of 2.04 eV to the Mo$_8$O$_{26}$ cluster, leading to electron rearrangement at the interface of the heterojunction (Fig. 7h). Specifically, Mo$_8$O$_{26}$-Nb$_4$N$_5$ exhibits a lower H$_2$O dissociation barrier (0.23 eV) compared to Nb$_4$N$_5$ (0.24 eV). The adsorption configuration of H$_2$O in the transition state (TS) reveals that the H$_2$O molecule is forced to significantly bend towards the Nb$_4$N$_5$ surface due to the cleavage of HO–H. At the Mo$_8$O$_{26}$-Nb$_4$N$_5$ interface, the H atom can be easily transferred to the O atom along the Nb–O–H···O–Mo hydrogen bond, which enhances the H$_2$O adsorption and reduces the H$_2$O dissociation barrier (Fig. 7i). The fully exposed multiple active sites within the Mo$_8$O$_{26}$ clusters exhibited an exceptional HER performance, surpassing that of the commercial Pt/C catalyst in pH-neutral electrolyte. Theoretical studies suggested that the electronic restructuring at the Mo$_8$O$_{26}$-NbN$_x$O$_y$ interface contributed to the optimal hydrogen adsorption energy and enhanced initial H$_2$O adsorption. Additionally, the synergistic effect between the terminal oxygen atoms in the Mo$_8$O$_{26}$ clusters and Nb atoms promoted the initial H$_2$O adsorption, reduced the H$_2$O dissociation energy, and accelerated the overall HER kinetics. Hu *et al.* employed a hydrothermal method using Na$_2$MoO$_4$·2H$_2$O as the Mo source to load nano-pom-pom multiphasic MoS$_2$ (NP-MoS$_2$) on carbonized wood (CW).[132] The unique structure of the NP-MoS$_2$/CW composite involved the stacking of MoS$_2$ sheets in a nanoscale pom-pom form grown on the CW substrate. The excellent electrical conductivity of CW compensated for the poor conductivity of MoS$_2$, and the synergistic effect between NP-MoS$_2$ and CW optimized the HER performance. NP-MoS$_2$/CW exhibited an outstanding electrocatalytic performance at $j = 10$ mA cm^{-2}, with overpotentials of 109.5 mV in 0.5 M H$_2$SO$_4$ and 140 mV in 1.0 M KOH.

To enhance electrocatalytic activity, Sakthinathan *et al.* employed a layer-by-layer (LbL) technique to attach nano-sized POM to a glassy carbon electrode (GCE), Na$_{0.3}$[N(C$_4$H$_9$)$_4$]$_{7.7}$[(Mo$_3$O$_8$)$_4$(O$_3$PC(O)(C$_3$H$_6$NH$_2$CH$_2$C$_4$H$_3$S)PO$_3$)$_4$] [(TBA)Mo$_{12}$(Alethio)$_4$].[133] The introduction of

polyethyleneimine (PEI) not only improved the conductivity and electrocatalytic activity of [(TBA)Mo$_{12}$(Alethio)$_4$], but also served as a supporting material for the formation of closely interconnected nanolayers. The nanolayer electrode exhibited a significant synergistic effect between the POM and positively charged PEI, leading to high electrocatalytic activity in 0.5 M H$_2$SO$_4$, with a small initial potential of approximately -0.077 V and a low Tafel slope of 80 mV dec^{-1} at $j = 10$ mA cm^{-2}.

4.1.4 Evans–Showell-type POM-based nanostructures. The approach of restricting the growth environment of materials to control their size has gained significant recognition in the field of electrocatalysis. By manipulating factors such as coordination bonds, organic cations, and mesoporous structures, researchers can effectively regulate the size and morphology of materials. This precise control of the material size allows for fine-tuning of the surface area of electrocatalysts, thus influencing their electrocatalytic performance. For example, Yue *et al.* implemented a multi-level spatial confinement strategy utilizing an Evans–Showell-type POM [Co$_2$Mo$_{10}$O$_{38}$H$_4$] as the precursor to encapsulate oxygen vacancy-rich 1T-MoS$_2$ (1T-Co-MoS$_2$) with highly dispersed cobalt species, resulting in particle sizes of less than 5 nm.[134] The Co–S edge sites were identified as the most active sites in the 1T-Co-MoS$_2$ catalyst, emphasizing the importance of cobalt doping. The Co-doped 1T-MoS$_2$ sites exhibited impressive intrinsic activity, abundant exposed active sites from the dispersed nanosheets, and enhanced charge and mass transfer within the hollow mesoporous carbon sphere (HMCS) substrate, collectively leading to superior HER activity. The resulting 1T-Co-MoS$_2$@HMCS catalyst demonstrated remarkable electrocatalytic activity for HER, with overpotentials of 220 mV and 245 mV in 1 M KOH and 0.5 M H$_2$SO$_4$, respectively, to achieve $j = 200$ mA cm^{-2}. Similarly, Ma *et al.* synthesized highly active CoS$_2$-MoS$_2$ nanocomposites using an Evans–Showell-type POM as the precursor under hydrothermal conditions.[135] The introduction of Co^{2+} effectively enhanced the exposure of active sites in MoS$_2$, thereby increasing the catalytic surface area. These examples demonstrate that Co doping improved the limited electrical conductivity of MoS$_2$, further enhancing the catalytic activity and structural stability, and ultimately optimizing the HER performance.

4.1.5 Summary. As shown in Table 1, isopolymolybdates exhibit superior electrocatalytic performances compared to other POM-based catalysts. Here, we systematically summarized the differences in the HER performance between iso-polymolybdates and other types of iso-POMs loaded on nanostructured materials to select the most suitable nanomaterials for different POMs. Taking the example reported by Yang *et al.*, they selected a conductive interface similar to Nb$_4$N$_5$ and a polyoxometalate [Mo$_8$O$_{26}$]$^{4-}$ with a significant electronegativity difference compared to the interface material to form a heterogeneous structure.[131] Based on the comprehensive analysis, we provide the following recommendations: (I) choose iso-POMs with a large difference in electronegativity from the conductive material for electrocatalytic HER reactions. (II) Consider the binding ability of the terminal O atoms in the POM structure, which depends on the rigidity of the metal–oxygen bonds. Therefore, MoO$_x$ clusters with exposed O atoms

This journal is © The Royal Society of Chemistry 2024

J. Mater. Chem. A, 2024, **12**, 13576–13604 | **13593**

should be the optimal choice for constructing chemically coupled heterogeneous interfaces with appropriate geometric and electronic structures. This optimizes the adsorption of H and H_2O and reduces the dissociation energy barrier of H_2O, thus synergistically improving the HER performance across the entire pH range.

4.2 Oxygen evolution reaction

Water oxidation is a crucial process in the fields of renewable energy and sustainable fuel production.[136] It involves the conversion of water molecules into oxygen, protons, and electrons. Due to the sluggish kinetics of the electrochemical water splitting reaction, there has been a greater focus in the past few decades on developing efficient OER electrocatalysts to improve the electrode kinetics and stability under different electrolyte conditions.[137] In recent years, significant efforts have been devoted to developing highly active and stable water oxidation catalysts, including incorporating POMs in surface-modified nanostructures. The high surface area and well-defined active sites of POMs contribute to improved catalytic performances. This high activity allows water molecules to efficiently release oxygen, making them promising catalysts for the water oxidation reaction.[138] Meanwhile, their robust structures and strong metal–oxygen bonds ensure that the catalyst remains intact and

active over long catalytic cycles. This stability is crucial for long-term catalytic performance and durability. More importantly, the characteristics of POM-based nanostructures provide high surface areas, facilitating the effective mass transfer of reactants and products.[139] This promotes the accessibility of reactants to the active sites of the catalyst and enhances its overall catalytic efficiency.

4.2.1 Anderson-type POM-based nanostructures. Anderson-type POMs are highly regarded as excellent nano-inorganic building blocks for the construction of multifunctional hybrid materials due to their ease of covalent modification. In 2022, Joshi et al. conducted pioneering research on the OER performance of Anderson cluster solids and improved their competitiveness through integration with acetylene black (AB).[136] A novel Anderson coordination compound, $[\{Co(2-pzc)(H_2O)_2\}_2\{H_7AlMo_6O_{24}\}] \cdot 10H_2O \cdot 2.5CH_3OH$ (PS-13), was synthesized. Subsequently, a series of composite materials was prepared by mechanically grinding PS-13 with acetylene black at a ratio of 1 : 2, resulting in an approximately 10% improvement in OER performance upon integration with AB. The AB&PS-13 composite material exhibited a significant catalytic OER performance in 1 M KOH, with the AB&PS-13 composite demonstrating a stable overpotential of 330 mV at $j = 10$ mA cm^{-2} and Tafel slope of 90 mV dec^{-1} over a 40 h period. In another study by Zhang et al., an Anderson-type POM,
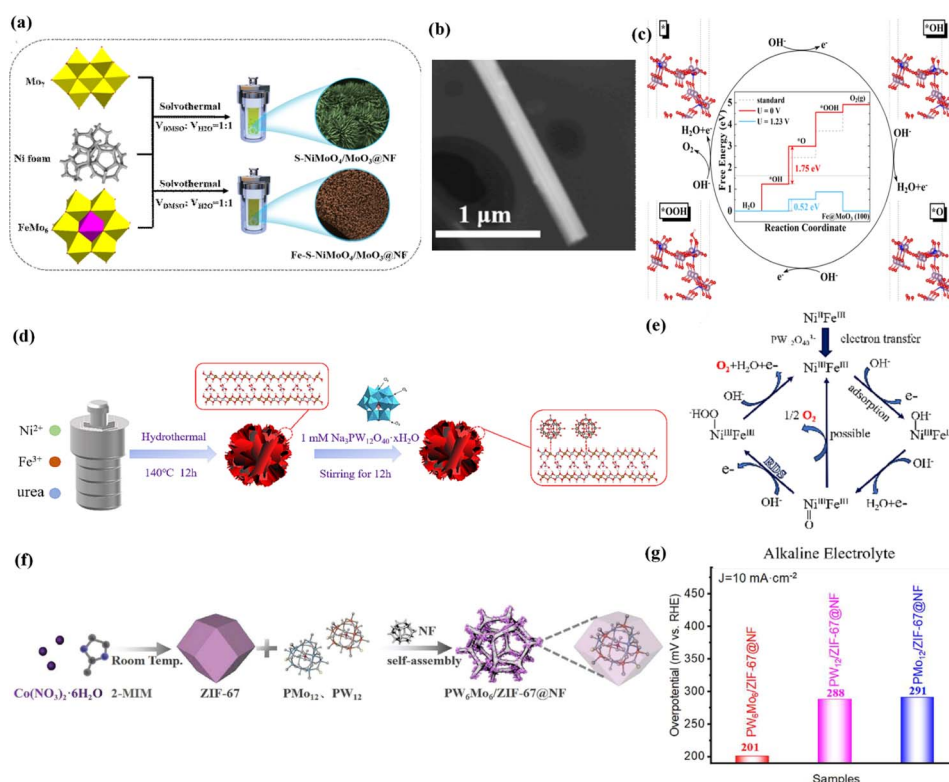

Fig. 8 (a) Schematic map of the synthesis of S-NiMoO$_4$/MoO$_3$@NF and Fe-S-NiMoO$_4$/MoO$_3$@NF electrodes. (b) HAADF-STEM of Fe-S-NiMoO$_4$/MoO$_3$@NF. (c) Free energy diagrams of Fe@MoO$_3$(100) for the OER process. Reproduced from ref. 137. Copyright 2021, Elsevier B.V. All rights reserved. (d) Schematic illustration of synthesis of NiFe-LDH-PW$_{12}$-12 h. (e) Mechanism of NiFe-LDH-PW$_{12}$-12 h for OER in alkaline electrolyte. Reproduced from ref. 138. Copyright 2023, Elsevier Inc. All rights reserved. (f) Process for the synthesis of PW$_6$Mo$_6$/ZIF-67@NF. (g) Comparison of overpotential of PW$_6$Mo$_6$/ZIF-67@NF, PW$_{12}$/ZIF-67@NF and PMo$_{12}$/ZIF-67@NF. Reproduced from ref. 146. Copyright 2023, Hydrogen Energy Publications LLC. Published by Elsevier Ltd. All rights reserved.

13594 | J. Mater. Chem. A, 2024, 12, 13576–13604

This journal is © The Royal Society of Chemistry 2024

$(NH_4)_3[FeMo_6O_{24}H_6]\cdot7H_2O$, was used as a precursor to fabricate binder-free Fe-S-NiMoO$_4$/MoO$_3$ electrodes *via* a solvothermal method (Fig. 8a).[137] These electrodes exhibited uniform growth on a nickel foam (NiF) in the form of a nanorod array (Fig. 8b). The DFT results demonstrated effective control of the OER process at each step through the presence of Fe heteroatoms (Fig. 8c). The ΔG_1 value in Fe@MoO$_3$(100) increases to 1.23 eV, indicating the weakened adsorption of *OH. Consequently, the potential-determining step on the surface of Fe@MoO$_3$(100) shifts to step 2, which involves the conversion of *OH to *O. Importantly, after Fe doping, the overpotential for this step is reduced to 0.52 V, indicating a significant enhancement in OER activity. According to the above-mentioned conclusions, the introduction of Fe doping facilitated the adjustment of the MoO$_3$ crystal facets, modulation of the electronic structure and enhancement of conductivity, thereby accelerating the reaction kinetics of OER. The Fe-S-NiMoO$_4$/MoO$_3$@NF electrode achieved an overpotential of 271 mV at $j = 500$ mA cm^{-2}. Overall, these studies highlight the promising potential of Anderson-type POMs and their derivatives in advancing the field of electrocatalysis, particularly in the context of the oxygen evolution reaction.

4.2.2 Saturated Keggin-type POM-based nanostructures. Saturated Keggin-type POMs, as precursors, exhibit prominent features such as high ion charge density, multifunctionality, and remarkable stability, which have attracted significant interest from the scientific community. Precise control of the electronic structure and electrocatalytic performance of NiFe layered double hydroxides (NiFe-LDHs) can be achieved through the coordination between adjacent metal sites and POMs. In the study by Shi *et al.*, NiFe-LDH-PW$_{12}$-X catalysts with varying modification times were prepared using the traditional hydrothermal method (Fig. 8d).[138] As the modification time increased, the ratio of Ni^{3+}/Ni^{2+} and the OER performance were gradually adjusted, demonstrating precise control of the active Ni sites by the "POM electronic sponge" on a temporal scale. POMs exhibited a strong electron-inductive effect and possessed high negative charge. During the modification process, POMs adsorbed on the Fe sites of the LDH layer, resulting in the transfer of electrons from the Ni sites to POMs. Consequently, Ni^{2+} was converted to Ni^{3+}, thereby modulating the electronic structure of the active Ni sites (Fig. 8e). Notably, NiFeLDH-PW$_{12}$-12 h underwent 12 h of PW$_{12}$ modification, which exhibited the highest OER performance characterized by rapid electron transfer, optimized reaction kinetics and excellent electrochemical stability. The overpotential of this catalyst was reduced by approximately 68 mV compared to the original NiFe-LDH. Li *et al.* synthesized two novel POM-based bisimidazole (H$_2$biim) complexes, [Ag(H$_2$biim)$_2$]$_2$[Ag$_4$(H$_2$biim)$_4$][(PW$_{12}$O$_{40}$)$_2$] and [Ag(H$_3$biim)$_2$][PW$_{12}$O$_{40}$]·4H$_2$O, *via* the hydrothermal method. By utilizing these compounds as precursors, two highly dispersed POM/Ag/graphene composites (designated as PW$_{12}$/Ag/graphene-a and PW$_{12}$/Ag/graphene-b, respectively) were successfully prepared, which involved modifying graphene as a carrier and utilizing DMF as a reducing agent.[139] These two composites exhibited excellent electrocatalytic ability for water oxidation in neutral media, which can be attributed to the

synergistic interface charge transfer among the three components, resulting in a better OER performance compared to pairwise combinations of other starting materials.

The utilization of MOF encapsulation to facilitate the interaction between POMs and MOFs is also a common strategy for the preparation of electrocatalysts. Liu *et al.* synthesized {Cu$_2$SiW$_{12}$O$_{40}$}@HKUST-1 using a conventional solution method.[140] The synergistic interaction between {Cu$_2$SiW$_{12}$O$_{40}$} and HKUST-1 promoted the charge transfer and adsorption/desorption of the intermediates on {Cu$_2$SiW$_{12}$O$_{40}$}@HKUST-1. As a result, this composite material exhibited excellent OER activity with a low overpotential (340 mV) and good cycling stability. Notably, {Cu$_2$SiW$_{12}$O$_{40}$}@HKUST-1 demonstrated a superior performance compared to commercial RuO$_2$. Zhao *et al.* synthesized carbon-supported metal oxides doped with PW$_{12}$, namely PW$_{12}$@amZIFs, *via* a series of chemical etching, cation exchange and thermal annealing steps using amorphous ZIF-67 as the precursor.[141] The synergistic effect of POMs and ZIF-67 resulted in an enhanced electrocatalytic OER performance. The resulting composite material exhibited a superior structure and composition, leading to a low overpotential (306 mV, $j = 10$ mA cm^{-2}) under OER conditions in 1.0 M KOH aqueous solution. Mukhopadhyay *et al.* were the first to report the used of an Fe-salen system for electrocatalytic OER. They prepared an efficient heterogeneous electrocatalyst, FSWZ-8 ((Fe-(salen)(OH) + H$_4$[SiW$_{12}$O$_{40}$]·HCl)@ZIF-8), by co-encapsulating Fe-salen (Fe(salen)Cl) and SiW$_{12}$ in the cavities of ZIF-8.[142] This catalyst achieved OER under neutral conditions. POMs in the system played a role in reducing the charge transfer resistance and lowering the overpotential, facilitating a higher loading of Fe-salen and making the synthesis of nanomaterials easier. This study revealed the significant potential of POMs in material synthesis.

The introduction of transition metals in the Keggin-type POM framework enables the formation of hybrid systems with unique properties and enhanced catalytic performances. Transition metals possess a range of desirable characteristics, such as variable oxidation states and high electron mobility, which can significantly influence the electrocatalytic processes. In 2020, Abdelkader-Fernández *et al.* reported the synergistic effect of incorporating cobalt-based POMs in Co-containing ZIF-67, which enhanced the OER process.[143] They synthesized two types of POM@ZIF nanocomposites, SiW$_9$Co$_3$@ZIF-8 and SiW$_9$Co$_3$@ZIF-67, using an *in situ* synthesis method at room temperature. These nanocomposites consisted of [SiW$_9$Co$_3$(H$_2$O)$_3$O$_{37}$]$^{10-}$ (SiW$_9$Co$_3$) encapsulated within the ZIF-8 and ZIF-67 frameworks, respectively. Although these nanocomposites had similar structures, they exhibited different OER performances. The ZIF-67 framework demonstrated a synergistic effect, whereas no significant effect was observed in ZIF-8. SiW$_9$Co$_3$@ZIF-67 showed a superior OER performance, which could be attributed to the electron transfer from ZIF-67 to POM and the complementation of Co^{2+} nodes on the POM framework. In the same year, Abdelkader-Fernández *et al.* synthesized SiW$_9$Co$_3$@ZIF-67 and SiW$_9$Co$_3$[h]@ZIF-67 nanocomposites by encapsulating SiW$_{11}$Co within the cavities of ZIF-67.[144] Compared to the previous study, the POM composition changed

This journal is © The Royal Society of Chemistry 2024

J. Mater. Chem. A, 2024, **12**, 13576–13604 | **13595**

with a lower Co^{2+} doping content. Despite their complex structure, according to the complete characterization of these high-POM-loaded materials, both nanocomposites exhibited enhanced OER activity compared to the original ZIF-67 framework, confirming previous findings. The improved OER performance of the nanocomposites with reduced Co^{2+} doping can be attributed to the presence of a higher quantity of POM clusters in the electrocatalyst and the significant structural modifications of the ZIF framework, which exposed more active sites.

Other transition metal-substituted POMs have also been studied. For example, Mulkapuri *et al.* synthesized a $\{Bi(OH_2)_2\}^{3+}$-functionalized Keggin-type POM compound, K_5-$[Bi(H_2O)_2SiW_{11}O_{39}]\cdot13H_2O$ ($K_51\cdot13H_2O$), as a precursor and encapsulated it within the cavities of zeolitic imidazolate framework ZIF-8.[145] The resulting host–guest-type composite, $H_5[Bi(H_2O)_2SiW_{11}O_{39}]@ZIF8$ ($H_51@ZIF8$), exhibited efficient electrocatalytic activity for water oxidation over a wide pH range (pH = 4.0–13.0). The $\{Bi(OH_2)_2\}^{3+}$ moiety on the surface of the POM acted as the active site for electrocatalytic water oxidation. The experimental results also indicated that the bismuth–water complexes served as the active sites for OER. Furthermore, the OER performance was influenced by modulating the electronegativity of the coordinated metal ions. Song *et al.* prepared PW_6Mo_6/ZIF-67@NF as an OER electrocatalyst using a simple co-precipitation method.[146] The introduction of PW_6Mo_6 induced the exposure of the Co nodes in ZIF-67, which acted as catalytic active sites for OER (Fig. 8f). The incorporation of PW_6Mo_6 improved the conductivity and electrochemically active surface area of ZIF-67, resulting in an ultra-low overpotential of 201 mV at $j = 10$ mA cm^{-2} (Fig. 8g).

4.2.3 Vacant Keggin-type POM-based nanostructures.

Vacant Keggin-type POMs display heightened catalytic activity owing to the presence of structural vacancies. These vacancies give rise to distinct active sites, facilitating an efficient charge transfer process and resulting in an enhanced electrocatalytic performance. Consequently, vacant Keggin-type POMs can be employed as promising precursors for the synthesis of nanomaterial-level electrocatalysts due to their exceptional electrocatalytic properties. Ahmed *et al.* employed 3-aminopropyl triethoxysilane (APTS) as a chemical linker to immobilize a high-nuclearity POM, $Na_{30.5}K_{1.5}[\{Co_4(OH)_3PO_4\}_4(A-\alpha-GeW_9O_{34})_4]\cdot116H_2O$ (Co_{16}-GeW_9), on NiF and investigated its electrocatalytic activity for OER.[147] The OER performance of Co_{16}-GeW_9@NiF was evaluated in both 1 M KOH solution (pH = 14) and sodium phosphate buffer solution (pH = 7). The catalyst exhibited an overpotential of 370 mV ($j = 10$ mA cm^{-2}) and Tafel slope of 84 mV dec^{-1} in 1 M KOH. In sodium phosphate buffer solution, the overpotential was 530 mV ($j = 10$ mA cm^{-2}) with a Tafel slope of 153 mV dec^{-1}. Lee *et al.* reported, for the first time, the effective OER performance of RuPOM deposited on carbon-supported graphite (KB) electrodes using a simple slurry coating method.[148] Notably, the RuPOM/KB composite demonstrated superior activity compared to commercial Pt/C. The utilization of RuPOM enabled the development of high-efficiency seawater batteries (SWBs) by significantly reducing the charging potential. The enhanced OER activity of the

RuPOM/KB composite could be attributed to the increased surface area provided by the vacant POM, which exposed more active sites. Additionally, the choice of a conductive carrier improved the overall conductivity of the composite material.

4.2.4 Finke-type POM-based nanostructures.

Finke-type POM clusters consist of metal oxide cores surrounded by oxygen atoms and coordinated ligands. The sandwich-like structure, together with the presence of a transition metal center, imparts distinct redox properties and catalytic activity. When integrated into nanostructures, these clusters exhibit enhanced performances and can be customized for specific applications. Gong *et al.* introduced the concept of molecular integration in materials by employing PEI as a chemical linker to connect the Finke-type POM $[Co_4(H_2O)_2(PW_9O_{34})_2]^{10-}$ and commercial titanium dioxide (P25) nanoparticles as molecular precursors.[149] The resulting nanomaterial exhibited remarkable self-activation behavior in 0.1 M KOH solution. This behavior could be attributed to the presence of highly active cobalt oxide and/or hydroxide catalysts, an increase in the electrocatalytic active surface area and improved conductivity, ultimately leading to a reduction in the overpotential for OER. This study demonstrated the significant enhancement in OER performance through the self-activation behavior of the catalyst. Abdelkader-Fernández *et al.* developed four novel ternary composite materials, namely $Co_4(PW_9)_2$@Co@C, $Co_4(PW_9)_2$@Co/Ni@C, $Co_4(PW_9)_2$@N, S-Co@C and $Co_4(PW_9)_2$@N,S-Co/Ni@C, by utilizing four different MOF-74-derived carbon-based nanocarriers in conjunction with the Finke-type POM $[Co_4(H_2O)_2(PW_9O_{34})_2]^{10-}$ ($Co_4(PW_9)_2$).[150] The comparative analysis revealed that the integration of Co/Ni@C carriers with POM induced partial structural modifications in both materials. This led to an increase in the surface area of the electrocatalyst but a decrease in its intrinsic OER activity. Alternatively, N,S-doped carbon carriers resulted in the higher immobilization of $Co_4(PW_9)_2$, leading to a reduction in its electrochemically active surface area but a significant enhancement in its inherent OER activity. This anomalous behavior could be attributed to the varying loading of $Co_4(PW_9)_2$ on the nanocomposite carriers, where the surface positions of $Co_4(PW_9)_2$ nanocrystals with highly accessible active sites for OH^- adsorption synergized with the inherent significant activity of the N,S-Co@C carrier. Additionally, as the OER proceeded at higher overpotentials, an increase in the coverage of O_2 molecules on the electrocatalyst surface was observed. This work also highlights the possibility that the excessive coverage of transition metals on different nanocarrier materials may lead to the reduced coverage of POM, resulting in the loss of more active sites.

4.2.5 Summary.

In the field of POM-based nanostructures, most research efforts have been focused on studying the OER performance of Keggin-type POMs based on W (Table 2). To improve their performance, researchers have explored the incorporation of transition metals. After introducing Co or Ni, the Tafel slope decreases significantly reaching the desired kinetic levels. However, their high overpotentials still remain an area that needs improvement. Recently, Song *et al.* prepared $PW_{12-n}Mo_n$/ZIF-67@NF ($n = 0, 3, 4, 6, 8, 9$ and 12) to investigate the enhancement in OER performance by tuning the W/Mo

ratio.[146] Here, we deduce possible reasons for the observed effects from the analysis of this structure, as follows: (I) the structure of PW_6Mo_6 is formed by an alternating arrangement of W and Mo atoms. It provides more active sites and a larger surface area, thereby increasing the opportunities and efficiency of catalytic reactions. In contrast, $PW_{12-n}Mo_n$ (n = 0, 3, 4, 8, 9 and 12) structures have fewer active sites and limited catalytic performance due to their imbalanced arrangement of W and Mo atoms or relatively simpler atomic arrangements. (II) PW_6Mo_6 is composed of W and Mo atoms, which show the advantage of superior electron conductivity compared to other transition metal compositions. They can efficiently transfer electrons, providing better electron conduction pathways. (III) The structure of PW_6Mo_6 exhibits high stability, maintaining its integrity and activity during catalytic reactions. This structural stability allows PW_6Mo_6 to maintain an efficient catalytic performance over prolonged reaction periods. Experimental results indicate that favorable OER performances can only be observed when the POM is PW_6Mo_6. Therefore, POMs in the form of Keggin-type with coordinating atoms as XW_6Mo_6 are currently considered the optimal choice for OER. Additionally, introducing heteroatoms to modify the structure of POMs offers an interesting avenue for future research.

4.3 CO$_2$ reduction

Carbon cycling is achieved by reducing carbon dioxide into valuable products, which also helps reduce the dependence on fossil fuels.[151] Electrocatalytic CO_2 reduction utilizes electrical energy as a power source and employs catalysts to facilitate the reduction of CO_2 molecules. This method allows the conversion of CO_2 under mild conditions and enables the selective synthesis of various organic compounds. However, electrocatalytic CO_2 reduction faces several challenges. (I) CO_2 is a highly stable molecule, and thus its catalytic reduction reaction needs to overcome high energy barriers.[152] (II) CO_2 reduction reactions often compete with oxidative side reactions, resulting in low product selectivity.[153] (III) Effective catalyst design and understanding the catalytic mechanisms are crucial areas that need to be studied.[154] Thus, to address these challenges, researchers have extensively explored various catalyst systems, including noble metals, non-noble metals and organic catalysts. Noble metal catalysts such as copper, silver and gold exhibit good electrocatalytic activity for CO_2 reduction, but their high cost and scarcity limit their application. Non-noble metal catalysts such as metal oxides, carbon-based materials, and polymers have broader resources and lower costs but require further improvement in terms of activity and selectivity. Organic catalysts, with their diverse structures and reaction properties, have emerged as promising catalyst systems, although their stability and efficiency still need improvement. POMs exhibit rich redox properties, tunable active sites, good selectivity and stability, making them attractive as both homogeneous and heterogeneous electrocatalysts for promoting the multi-electron reduction of CO_2 into useful chemicals. Currently, nanostructured POM-based materials as CO_2 reduction catalysts have received considerable attention.

4.3.1 Saturated Keggin-type POM-based nanostructures. The use of POMs and monometallic or metal-coordinated complexes in the field of electrocatalysis has attracted significant attention. Sun et al. developed a series of mixed-valence POM@MOF composite materials by modifying POMs with transition metals (Fig. 9a).[152] Among these composites, H-POM@PCN-222(Co) exhibited enhanced electron transfer capability, enabling efficient CO_2RR with an exceptional FE_{CO} = 96.2% and good stability over 10 h (Fig. 9b). This report proves that introducing POM into PCN-222 (Co) can lead to several advantages, as follows: (I) it can anchor itself to Co-TCPP. (II) It establishes a directed electron transfer pathway to the mononuclear site of Co, thereby accelerating electron transfer in this multi-metallic system. (III) By enriching the electron density of the Co center in the monometallic site, the introduction of POM in PCN-222 (Co) effectively reduces the energy barrier of the rate-determining step (RDS) from *CO_2 to *COOH. This results in a significant enhancement in the catalytic activity for CO_2RR (Fig. 9c). Yang et al. synthesized bilayered nanosheets of Zn-CoTAPc by incorporating a POM (PMO_{12}) into zinc-metalloporphyrins (MPc).[153] These nanosheets showed highly exposed Co active sites and a well-stacked structure, leading to improved electrocatalytic and photo-assisted electrocatalytic CO_2 reduction. The introduction of POM prevented the aggregation of MPc molecular layers, allowing for better exposure of the active centers. Under light irradiation, the nanosheets exhibited optimized electron transfer pathways for CO_2 molecules, facilitating efficient electron transmission from the Co metal center and impeding HER. The nanosheet structure also promoted the efficient separation of photogenerated carriers, resulting in a twofold increase in electrocatalytic efficiency under applied bias conditions. Du et al. reported the synthesis of POM-based carbonyl manganese (MnL) composite electrocatalysts (POM-MnL) with SiW_{12}-MnL, exhibiting the highest activity and selectivity for CO_2 reduction to CO.[154] The POM component facilitated electron transfer from POM to the MnL units, enhancing the selectivity for CO_2RR toward CO and suppressing the competing HER.

Although indium (In) electrodes are widely used as electrochemical catalysts due to their excellent properties, the complex reaction pathways and high overpotentials associated with In electrocatalytic CO_2RR pose challenges. In this case, due to the ability of POMs to transport and store electrons and protons, they show great potential for overcoming these limitations. The choice of coordinating metal atoms also influences the electrocatalytic processes, which is also an important factor worthy of attention. Sun et al. investigated the impact of V and Mo on CO_2RR by combining In electrodes with different Keggin-type POMs ($PV_nMo_{(12-n)}O_{40}^{(n+3)-}$, n = 1, 2, 3) (Fig. 9d).[155] The V atoms in the POM facilitated CO_2 adsorption, while the Mo atoms played a role in electrode oxidation. However, the oxidation of Mo resulted in the loss of active sites on the In electrode, leading to the weak adsorption of *CO during electrolysis. In the PV_3Mo_9 system, the high proportion of active sites to electrode surface promoted C–C coupling and the production of the C_2 product ethanol (Fig. 9e). Zha et al.
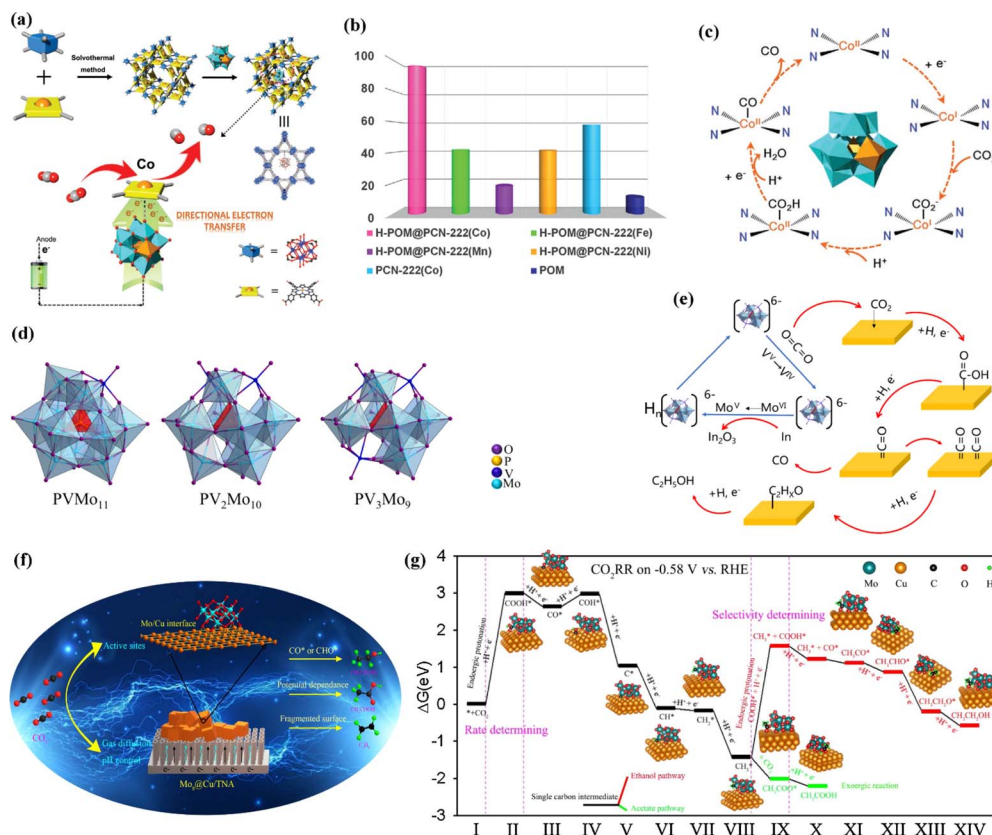
Fig. 9 (a) Top: Schematic of the synthetic process and the detailed structure of POM@PCN-222(Co) composite. Bottom: Proposed electron-transfer scheme on the active single-metal site Co of H-POM@PCN-222(Co) for CO_2RR. (b) Maximum FE_{CO} for six samples at -0.8 V (vs. RHE). (c) Mechanism of CO_2RR in H-POM@PCN-222(Co). Reproduced from ref. 152. Copyright 2021, Wiley-VCH GmbH. (d) Crystal structures of $PVMo_{11}$, PV_2Mo_{10} and PV_3Mo_9. (e) Mechanism scheme of POM and indium synergistic catalysis of CO_2RR. Reproduced from ref. 155. Copyright 2023, Elsevier Inc. All rights reserved. (f) Schematic diagram of electrochemical CO_2 reduction reaction with $Mo_8@Cu/TNA$. (g) Free energy diagrams and reaction pathway of CO_2RR with $Mo_8@Cu/TNA$ under -0.58 V vs. RHE. Reproduced from ref. 157. Copyright 2020, Elsevier B.V. All rights reserved.

demonstrated the crucial role of V centers in POM for the conversion of CO_2 to C_2 products.[156] By combining Keggin-type POM $[SiW_9V_3O_{40}]^{7-}$ (SiW_9V_3) with In, the efficient reduction of CO_2 to acetic acid and formic acid was achieved with high FE (96.5%). These findings highlight the potential of POM electrolyte additives for regulating the microenvironment to enhance the CO_2RR performance.
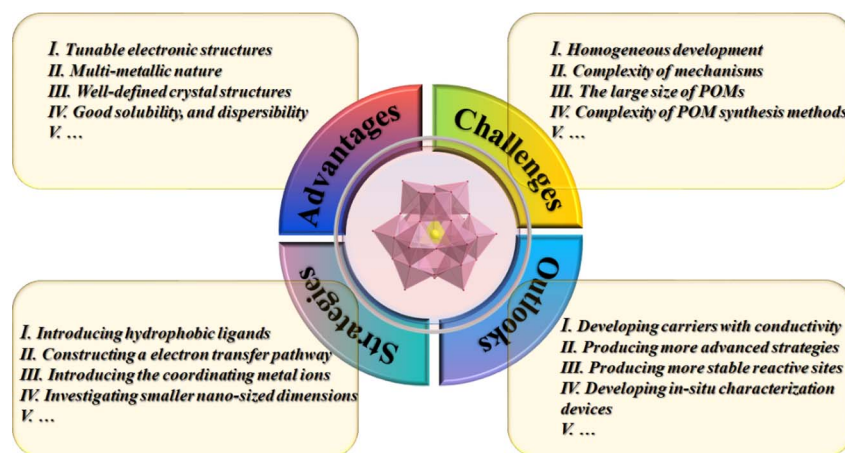
4.3.2 Isopolyoxomolybdate-based nanostructures. When the distribution of elements on a composite material is uneven, it can lead to continuous coupling reactions. Zang et al. reported on the synthesis of a POM-modified copper nanocube $Mo_8@Cu/TNA$ composite material, which formed a Cu–O–Mo interface as the active site for CO_2RR (Fig. 9f).[157] The use of titanium nanotubes (TNA) as the carrier facilitated CO_2 diffusion and controlled local pH changes due to their nanoscale length and density, resulting in significantly enhanced electrocatalytic activity and stability. Furthermore, the composite material exhibited both a remarkable electron reservoir and proton transfer capabilities associated with POM, as well as synergistic effects between Mo_8 and Cu. Interestingly, during the CO_2RR process, the presence of different multi-carbon products was observed. These products originated from the

fragmented Cu regions that were not covered by the Cu–O–Mo interface. The proposed current single-carbon coupling pathway, as shown in Fig. 9g, involves the formation of acetate through the coupling of a CO_2 molecule with *CH_3, followed by two consecutive exothermic reactions. This can be attributed to the Cu–O–Mo interface induced by the Mo_8 cluster on the Cu surface, which modulates the electrochemical selectivity of CO_2RR towards acetate. Under all the applied potential conditions, the generation of ethanol must undergo an endothermic protonation step to complete the formation of the C–C bond, which strongly suppresses its selectivity as the determining step. However, the final free energy of ethanol is lower than acetate at -1.13 V vs. RHE (-6.61 V for acetate and -7.18 V for ethanol). The interaction between these Cu regions and the POM at the interface, which was rich in Cu–O–Mo active sites, facilitated the generation of intermediate *CH_3 and the continuous coupling of CO_2 insertion.

4.3.3 Summary. The exploration of POM-based single-crystal structures in CO_2RR is limited, and thus we discussed single-crystal and nanostructured catalysts together. The experimental results presented in Table 3 highlight the broad application of Keggin-type catalysts in CO_2 reactions and the

Table 3 A summary of the POM-based electrocatalysts for electrocatalytic CO_2RR presented in this review

Type of POM	Electrocatalyst	Electrolyte	Potential	Principal product	FE (%)	Ref.
Keggin	Fe-POMOFs (Zn-ε-Keggin)	0.5 M $KHCO_3$	−0.71 V (vs. RHE)	CO	92.1	115
	POM@PCN-222(Co) ($CoW_{11}Co$)	0.5 M $KHCO_3$	−0.8 V (vs. RHE)	CO	96.2	152
	Zn-CoTAPc/PMo_{12}	0.5 M $KHCO_3$	−0.7 V (vs. RHE)	CO	96.1	153
	SiW_{12}-MnL/KB	0.5 M $KHCO_3$	−0.72 V (vs. RHE)	CO	95	154
	PW_{12}-MnL/KB	0.5 M $KHCO_3$	−0.72 V (vs. RHE)	CO	80	154
	PMo_{12}-MnL/KB	0.5 M $KHCO_3$	−0.52 V (vs. RHE)	CO	65	154
	$PVMo_{11}$ + In	0.1 M Na_2SO_4	−0.5 V (vs. RHE)	C_2H_5OH	53	155
	PV_2Mo_{10} + In	0.1 M Na_2SO_4	−0.3 V (vs. RHE)	C_2H_5OH	80	155
	PV_3Mo_9 + In	0.1 M Na_2SO_4	−0.3 V (vs. RHE)	C_2H_5OH	93.4	155
	PMo_{12} + In	0.1 M Na_2SO_4	−0.6 V (vs. RHE)	C_2H_5OH	29.6	155
	SiW_9V_3 + In	0.1 M Na_2SO_4	−0.71 V (vs. RHE)	CH_3COOH	96.5	156
Isopolyoxomolybdates	Mo_8@Cu/TNA	The saturated $NaHCO_3$	−0.71 V (vs. RHE)	CH_3COOH	88.94	157
		The saturated $NaHCO_3$	−0.71 V (vs. RHE)	CH_4	14.42	157
		The saturated $NaHCO_3$	−0.71 V (vs. RHE)	C_2H_4	28.34	157

Fig. 10 Schematic illustration of the advantages, challenges, strategies and outlooks of POM-based electrocatalysts in practical applications.

role of coordinating atoms (Mo, V, W). In experiments with isopolymolybdates, encapsulating $[Mo_8O_{26}]^{4-}$ in a conductive material resulted in the generation of a significant amount of C1 or Cn ($n \geq 2$) products.[157] However, these products lacked selectivity, necessitating the exploration of POMs with better selectivity for the quantification of C1 or Cn ($n \geq 2$) products. Employing indium foil and V-substituted Keggin-type POMs in the electrocatalytic reaction setup achieved the stable generation of Cn ($n \geq 2$) products and significantly enhanced the FE.[155,156] This phenomenon can be attributed to the similarity between the electrocatalytic CO_2RR and HER processes, which often occur simultaneously. The electron transfer required for HER is typically lower than that required for carbon product generation, resulting in lower electron transfer impedance and higher current density for HER. Therefore, the presence of Mo coordinating atoms in POMs favors electron transfer in the HER process, leading to a reduction in C1 and Cn ($n \geq 2$) products during CO_2RR. The addition of V coordinating atoms to POMs significantly enhances C–C coupling and suppresses HER, making them an excellent electrolyte additive for modulating the electron transfer process in CO_2RR. Hence, for the directed synthesis of C2 products for resource utilization, the optimal

choice is Keggin-type POMs with a higher V content, such as PV_3Mo_9. Currently, research in the field of CO_2RR is limited, underscoring the importance of intensifying research efforts to generate valuable chemicals and clean energy.

5. Conclusions and outlooks

Herein, we presented a comprehensive review of the research advancements in the field of POMs and their derivatives as a class of electrocatalysts for HER, OER, and CO_2RR, covering the period from 2020 to the present. This review was structured into two main sections, namely POM-based single-crystal structures and POM-based nanostructures. Within these sections, detailed discussions were presented on various structures, including giant clusters, assemblies, and organic–inorganic hybrid materials, with a specific focus on their correlation with electrocatalytic performance. Additionally, we extensively enumerated, summarized, and compared the effects and roles of different types of POMs in the field of electrocatalysis, with the ultimate aim of identifying the most suitable POM variants for electrocatalytic HER, OER, and CO_2RR applications. However, despite the significant progress achieved in

This journal is © The Royal Society of Chemistry 2024

J. Mater. Chem. A, 2024, 12, 13576–13604 | 13599

electrocatalysis for energy applications, there are still numerous problems that need to be addressed. In the subsequent sections, we provide a comprehensive discussion on the advantages, challenges, strategies, and outlooks in this domain (Fig. 10).

5.1 Advantages

POM-based electrocatalysts have tunable electronic structures and chemical compositions, facilitating electron transfer and promoting redox reactions to enhance the catalytic rates. Moreover, their multi-metallic nature allows for interconversion isomerism during catalytic processes, greatly facilitating the formation of the oxidation and reduction products required in most POM-based electrocatalysts for processes such as HER, OER, and CO_2RR. Reductive POMs play a significant role in CO_2RR, with the presence of vanadium enhancing their ability to reduce CO_2 to C_2 products. The desirable features of POMs, such as well-defined crystal structures, controllable morphologies, good solubility, and dispersibility, contribute to their popularity in the field of electrocatalysis. By summarizing the methods for the synthesis of the most efficient and stable POM-based electrocatalysts, we can roughly categorize them into the following five strategies:

(I) Self-assembly of POM components into multinuclear clusters, leading to numerous redox reactions;

(II) Introduction of transition metal ions as heteroatoms in POM derivatives to achieve controlled electronic structures and enhanced electron transfer;

(III) Incorporation of varying numbers of transition metal active sites into vacancy-containing POMs to create single-cluster electrocatalysts with fixed electron transfer;

(IV) Doping POM into MOFs with porous materials to achieve heterogenization and increased active sites; and

(V) Loading POM onto different types of conductive substrates to improve the conductivity of composite materials and enhance the catalytic surface area.

5.2 Challenges

POM-based electrocatalysts have made significant progress in the fields of HER, OER, and CO_2RR. However, there are still several challenges that need to be addressed and improved.

(I) Although POM molecules generally have good solubility and adhesion in practical applications, their homogeneous development is limited due to the challenge of separating POMs from the bulk material. Therefore, it is necessary to explore better methods that can overcome this challenge and allow for the more effective utilization of the catalytic performance of POMs.

(II) POMs can be loaded onto various conductive substrates to achieve heterogenization, greatly improving the conductivity of electrocatalysts. However, the lack of precise structural information and the complexity of mechanisms due to structural diversity make it difficult to accurately identify the active sites and reaction intermediates in these composite materials. Consequently, further research is needed to establish a better

understanding of the structure–performance relationship in POM composite materials.

(III) Both catalytic activity and stability are crucial factors for electrocatalysts. The large size of POMs poses a challenge in precisely controlling the size of POM molecules for better dispersion at interfaces or encapsulation within MOF frameworks, which can provide clear guidance for improving the stability.

(IV) POMs exhibit unique physicochemical properties, but current research on their CO_2RR activity is relatively limited. Therefore, extensive studies are needed to explore the impact of multi-metal/heterometallic synergistic effects in POMs on CO_2 reduction products.

(V) Many POM-based nanostructures and single-crystal structures have been reported as promising electrocatalysts for practical applications. However, the complexity of the methods for the synthesis POMs often limits their large-scale production in industrial settings. Therefore, the design of simpler synthetic routes plays a crucial role in achieving industrialization.

(VI) The attachment of POMs to a support matrix is crucial for maintaining their stability during the electrocatalytic process. However, achieving a strong and stable interface between the POMs and the support material can be challenging. Weak interactions or insufficient bonding can result in the detachment or leaching of POMs, leading to the loss of catalytic activity and reduced stability.

5.3 Strategies

To develop superior POM-based electrocatalysts, two key aspects that should be emphasized are improving their conductivity and stability. To achieve this, the following strategies can be employed:

(I) Introducing hydrophobic or highly conductive functional organic ligands to modulate the physicochemical properties of POM-based electrocatalysts through coordination, thereby enhancing their catalytic capabilities.

(II) Enhancing the binding ability between the conductive substrate and POM to facilitate effective adhesion, charge transfer, and stability. Constructing a well-defined electron transfer pathway, such as Cu–O–Mo, can also enhance the synergistic interaction between the substrate and POM.

(III) Saturated POMs often exhibit weak catalytic activity due to their saturated coordination systems. To enhance both the conductivity and the number of active sites, transition metal ions can be introduced in POMs with vacant sites. Altering the coordinating metal ions can also modify the catalytic activity. For example, replacing PMo_{12} with PMo_9V_3 has been shown to enhance the reduction ability of CO_2.

(IV) Investigating POM-based materials with smaller nano-sized dimensions is also important. The typical approach of grinding larger POMs into smaller sizes may damage their crystalline structure, making it challenging to accurately evaluate their catalytic activity. A more appropriate approach will be to incorporate effective modulators during the synthesis process to control their self-assembly. The common methods

13600 | *J. Mater. Chem. A*, 2024, **12**, 13576–13604

This journal is © The Royal Society of Chemistry 2024

for the fabrication of POMs include hydrothermal synthesis and solvothermal methods. Additionally, reducing the heating time can decrease the degree of molecular aggregation and reduce the size of POM particles.

(V) To prevent the detachment or leaching of POMs during the electrocatalytic process and enhance the stability between POMs and the support materials, a protective coating can be formed between them to prevent the contact of POMs with the external environment. This can be achieved through methods such as chemical deposition, sol–gel method, and electrochemical deposition. The protective coating can provide an additional protective barrier, maintaining the stability and activity of POMs.

5.4 Outlooks

The tunable redox properties and rapid electron transfer of POM-based electrocatalysts are closely related to their structural changes. Therefore, designing more rational nanocrystal structures holds great application prospects for efficient POM-based electrocatalysts in HER, OER, and CO_2RR, which is also a major development direction for future electrocatalysts.

(I) In addition to the inherent properties of POMs, it is important to develop carriers with better conductivity or encapsulate POMs in MOFs with higher porosity to enhance their electrocatalytic performance by increasing their conductivity and specific surface area.

(II) More advanced strategies and fabrication processes should be developed to enhance the cohesion between POMs and organic ligands or materials, thereby improving the stability of nanostructures and single-crystal structures.

(III) POMs demonstrate adjustable redox capabilities, and it is well-established that reducible POMs can enhance the efficiency of CO_2RR. More stable and accurate reactive sites should be constructed, which are conducive to the stable and efficient recovery of CO_2 reduction into specific products.

(IV) The presence of POMs can lead to synergistic effects, enhancing the electrocatalytic capabilities, while making the reaction mechanism more complex. Therefore, developing *in situ* characterization devices to monitor the dynamic structural changes in POM-based electrocatalysts during electrocatalytic reactions and revealing the precise catalytic reaction principles based on identifying reactive intermediates are crucial.

(V) It is important to develop more novel POM-based electrocatalysts with inherent strong electrocatalytic activity, rather than relying on the addition of other transition metals during the synthesis process to enhance electrocatalytic activity.

(VI) In the evaluation of the HER and OER performance, it has been observed that isopolyoxovanadates and isopolyoxomolybdates demonstrate a superior performance. However, their application as POM-based electrocatalysts remains limited. Therefore, it is urgent to use polyoxometalates with Mo and V as coordination atoms to develop POM-based single-crystal structures and nanostructures. These research directions hold great potential for advancing POM-based electrocatalysts with enhanced catalytic activity and stability.

(VII) The utilization of protective coatings and encapsulation techniques can provide effective protection for POMs against the influence of harsh electrochemical environments. The research and development of new coating materials and deposition methods are indispensable for further improving the stability of POM-based electrocatalysts.

Conflicts of interest

There are no conflicts to declare.

Acknowledgements

Notes and references

1 B. Li and N. Haneklaus, *Energy Rep.*, 2021, **7**, 783–791.
2 J. Kurtz, M. Peters, M. Muratori and C. Gearhart, *IEEE Electrific. Mag.*, 2018, **6**, 8–18.
3 X. Chang, T. Wang and J. Gong, *Energy Environ. Sci.*, 2016, **9**, 2177–2196.
4 S. Berardi, S. Drouet, L. Francas, C. Gimbert-Surinach, M. Guttentag, C. Richmond, T. Stoll and A. Llobet, *Chem. Soc. Rev.*, 2014, **43**, 7501–7519.
5 A. M. Liu, W. X. Guan, K. F. Wu, X. F. Ren, L. G. Gao and T. L. Ma, *Appl. Surf. Sci.*, 2021, **540**, 7.
6 C. He, C. Xu and W. X. Zhang, *ACS Appl. Mater. Interfaces*, 2023, **15**, 57015–57028.
7 H. Semai and A. Bouhdjar, *Environ. Sci. Pollut. Res.*, 2023, **30**, 52692–52701.
8 C. Y. Guo, Y. M. Shi, S. Y. Lu, Y. F. Yu and B. Zhang, *Chin. J. Catal.*, 2021, **42**, 1287–1296.
9 Z. F. Xin, J. J. Liu, X. J. Wang, K. J. Shen, Z. B. Yuan, Y. F. Chen and Y. Q. Lan, *ACS Appl. Mater. Interfaces*, 2021, **13**, 54949–54956.
10 C. Zhang, Y. Liu, J. M. Wang, W. P. Li, Y. L. Wang, G. H. Qin and Z. G. Lv, *Appl. Surf. Sci.*, 2022, **595**, 10.
11 P. Zhou, G. Y. Zhai, X. S. Lv, Y. Y. Liu, Z. Y. Wang, P. Wang, Z. K. Zheng, H. F. Cheng, Y. Dai and B. B. Huang, *Appl. Catal., B*, 2021, **283**, 9.
12 A. Krishnan, R. Ajay, J. Anakha and U. S. K. Namboothiri, *Surf. Interfaces*, 2022, **30**, 22.
13 G. Q. Zhang, Y. F. Zhou and F. L. Yang, *Electrochim. Acta*, 2019, **299**, 672–681.
14 H. L. Dong, Y. Y. Li and D. E. Jiang, *J. Phys. Chem. C*, 2018, **122**, 11392–11398.
15 Y. Qiao, W. C. Lai, K. Huang, T. T. Yu, Q. Y. Wang, L. Gao, Z. L. Yang, Z. S. Ma, T. L. Sun, M. Liu, C. Lian and H. W. Huang, *ACS Catal.*, 2022, **12**, 2357–2364.
16 Z. L. Zhao and G. Lu, *J. Phys. Chem. C*, 2019, **123**, 4380–4387.

This journal is © The Royal Society of Chemistry 2024

J. Mater. Chem. A, 2024, **12**, 13576–13604 | **13601**

17 Z. Y. Guo, F. B. Yang, X. T. Li, H. W. Zhu, H. Do, K. L. Fow, J. D. Hirst, T. Wu, Q. L. Ye, Y. Q. Peng, H. Bin Wu, A. J. Wu and M. X. Xu, *J. Energy Chem.*, 2024, **90**, 540–564.

18 Q. K. Fan, X. Zhang, X. H. Ge, L. C. Bai, D. S. He, Y. T. Qu, C. C. Kong, J. L. Bi, D. W. Ding, Y. Q. Cao, X. Z. Duan, J. Wang, J. Yang and Y. Wu, *Adv. Energy Mater.*, 2021, **11**, 2101424.

19 S. J. Li, Y. B. Ma, Y. Zhao, R. J. Liu, Y. P. Zhao, X. S. Dai, N. A. Ma, C. Streb and X. N. Chen, *Angew. Chem., Int. Ed.*, 2023, **62**, e202314999.

20 S. S. Wang and G. Y. Yang, *Chem. Rev.*, 2015, **115**, 4893–4962.

21 N. I. Gumerova and A. Rompel, *Nat. Rev. Chem*, 2018, **2**, 20.

22 L. L. Zhang, X. Ding, M. Y. Cong, Y. Wang and X. D. Zhang, *Int. J. Hydrogen Energy*, 2019, **44**, 9203–9209.

23 L. Yang, Z. Zhang, C. N. Zhang and X. L. Wang, *Rare Met.*, 2024, **43**, 236–246.

24 S. Bhatt and S. Saha, *Prog. Solid State Chem.*, 2023, **72**, 27.

25 L. Yang, Z. Zhang, C. N. Zhang and X. L. Wang, *Rare Met.*, 2023, **43**, 236–246.

26 J. M. Cameron, G. Guillemot, T. Galambos, S. S. Amin, E. Hampson, K. M. Haidaraly, G. N. Newton and G. Izzet, *Chem. Soc. Rev.*, 2022, **51**, 293–328.

27 M. R. Horn, A. Singh, S. Alomari, S. Goberna-Ferrón, R. Benages-Vilau, N. Chodankar, N. Motta, K. Ostrikov, J. MacLeod, P. Sonar, P. Gomez-Romero and D. Dubal, *Energy Environ. Sci.*, 2021, **14**, 1652–1700.

28 T. Ueda, *ChemElectroChem*, 2018, **5**, 823–838.

29 H. J. Lv, W. W. Guo, K. F. Wu, Z. Y. Chen, J. Bacsa, D. G. Musaev, Y. V. Geletii, S. M. Lauinger, T. Lian and C. L. Hill, *J. Am. Chem. Soc.*, 2014, **136**, 14015–14018.

30 S. Y. Lai, K. H. Ng, C. K. Cheng, H. Nur, M. Nurhadi and M. Arumugam, *Chemosphere*, 2021, **263**, 23.

31 J. F. Keggin, *Nature*, 1933, **131**, 908.

32 G. P. Yang, Y. F. Liu, K. Li, W. Liu, B. Yu and C. W. Hu, *Chin. Chem. Lett.*, 2020, **31**, 3233–3236.

33 D. Ye, R. Y. Qu, Y. X. Zhang, W. H. Wu, S. J. Liu, C. H. Zheng and X. Gao, *Mol. Catal.*, 2018, **448**, 177–184.

34 J. L. Jios, N. Metzler-Nolte, P. G. Vázquez and G. P. Romanelli, *Res. Chem. Intermed.*, 2016, **42**, 977–986.

35 W. W. He, S. L. Li, H. Y. Zang, G. S. Yang, S. R. Zhang, Z. M. Su and Y. Q. Lan, *Coord. Chem. Rev.*, 2014, **279**, 141–160.

36 C. L. Yue, F. Y. Sun, N. Liu, Y. Liu, W. J. Bao, X. W. Zhang, C. Zhang, S. Y. Ma, Y. Zhou, C. Feng and Y. K. Lu, *Fuel*, 2024, **357**, 129668.

37 A. Blazevic and A. Rompel, *Coord. Chem. Rev.*, 2016, **307**, 42–64.

38 N. V. Maksimchuk, V. Y. Evtushok, O. V. Zalomaeva, G. M. Maksimov, I. D. Ivanchikova, Y. A. Chesalov, I. V. Eltsov, P. A. Abramov, T. S. Glazneva, V. V. Yanshole, O. A. Kholdeeva, R. J. Errington, A. Solé-Daura, J. M. Poblet and J. J. Carbó, *ACS Catal.*, 2021, **11**, 10589–10603.

39 J. L. Liang, W. W. Wang, W. J. Wu, M. M. Wu, J. W. Hua, Y. Q. Liu and C. G. Liu, *ChemistrySelect*, 2023, **8**, e202300004.

40 X. L. Wang, R. Zhang, X. Wang, H. Y. Lin, G. C. Liu and H. X. Zhang, *Polyhedron*, 2017, **135**, 180–188.

41 W. G. Zhang, T. G. Zhang, G. Z. Lv, X. J. Cao and H. Y. Zhu, *Sep. Purif. Technol.*, 2019, **218**, 164–172.

42 B. Fabre, C. Falaise and E. Cadot, *ACS Catal.*, 2022, **12**, 12055–12091.

43 X. L. Yang, X. Y. Xie, S. Q. Li, W. X. Zhang, X. D. Zhang, H. X. Chai and Y. M. Huang, *J. Hazard. Mater.*, 2021, **419**, 12.

44 N. Li, J. Liu, B. X. Dong and Y. Q. Lan, *Angew. Chem., Int. Ed.*, 2020, **59**, 20779–20793.

45 J. J. Walsh, A. M. Bond, R. J. Forster and T. E. Keyes, *Coord. Chem. Rev.*, 2016, **306**, 217–234.

46 X. X. Li, D. Zhao and S. T. Zheng, *Coord. Chem. Rev.*, 2019, **397**, 220–240.

47 D. D. Li, P. T. Ma, J. Y. Niu and J. P. Wang, *Coord. Chem. Rev.*, 2019, **392**, 49–80.

48 L. W. Han, J. X. Lin, Q. Yin, B. Karadeniz, H. F. Li, J. Lü and R. Cao, *Cryst. Growth Des.*, 2016, **16**, 1213–1217.

49 Q. Gao, D. H. Hu, M. H. Duan and D. H. Li, *J. Mol. Struct.*, 2019, **1184**, 400–404.

50 T. V. Pinto, D. M. Fernandes, C. Pereira, A. Guedes, G. Blanco, J. M. Pintado, M. F. R. Pereira and C. Freire, *Dalton Trans.*, 2015, **44**, 4582–4593.

51 M. Choudhari, J. J. Xu, A. I. McKay, C. Guerrin, C. Forsyth, H. Z. Ma, L. Goerigk, R. A. J. O'Hair, A. Bonnefont, L. Ruhlmann, S. Aloise and C. Ritchie, *Chem. Sci.*, 2022, **13**, 13732–13740.

52 Y. Q. Jiao, C. Qin, X. L. Wang, C. G. Wang, C. Y. Sun, H. N. Wang, K. Z. Shao and Z. M. Su, *Chem. - Asian J.*, 2014, **9**, 470–478.

53 T. L. Lai, M. Awada, S. Floquet, C. Roch-Marchal, N. Watfa, J. Marrot, M. Haouas, F. Taulelle and E. Cadot, *Chem.–Eur. J.*, 2015, **21**, 13311–13320.

54 Y. L. Ren, L. Li, B. Mu, C. X. Li and R. D. Huang, *J. Solid State Chem.*, 2017, **249**, 1–8.

55 J. C. Liu, J. W. Zhao, C. Streb and Y. F. Song, *Coord. Chem. Rev.*, 2022, **471**, 23.

56 Z. B. Gan, J. S. Chen, J. Wang, C. M. Wang, M. B. Li, C. H. Yao, S. L. Zhuang, A. Xu, L. L. Li and Z. K. Wu, *Nat. Commun.*, 2017, **8**, 6.

57 M. Bugnola, K. J. Shen, E. Haviv and R. Neumann, *ACS Catal.*, 2020, **10**, 4227–4237.

58 A. M. Todea, A. Merca, H. Bögge, T. Glaser, J. M. Pigga, M. L. K. Langston, T. Liu, R. Prozorov, M. Luban, C. Schröder, W. H. Casey and A. Müller, *Angew. Chem., Int. Ed.*, 2010, **49**, 514–519.

59 W. Jiang, X. M. Liu, J. Liu, J. Shi, J. P. Cao, X. M. Luo, W. S. You and Y. Xu, *Chem. Commun.*, 2019, **55**, 9299–9302.

60 W. M. Xuan, R. Pow, N. Watfa, Q. Zheng, A. J. Surman, D. L. Long and L. Cronin, *J. Am. Chem. Soc.*, 2019, **141**, 1242–1250.

61 H. Y. Wang, S. R. Li, X. Wang, L. S. Long, X. J. Kong and L. S. Zheng, *Sci. China: Chem.*, 2021, **64**, 959–963.

62 Y. L. Wu, X. X. Li, Y. J. Qi, H. Yu, L. Jin and S. T. Zheng, *Angew. Chem., Int. Ed.*, 2018, **57**, 8572–8576.

63 Z. M. Wang, X. Xin, M. Zhang, Z. Li, H. J. Lv and G. Y. Yang, *Sci. China: Chem.*, 2022, **65**, 1515–1525.

13602 | *J. Mater. Chem. A*, 2024, **12**, 13576–13604

This journal is © The Royal Society of Chemistry 2024

64 A. A. Seddon, N. S. Hill, O. El-Zubir, A. Houlton, R. J. Errington, P. Docampo and E. A. Gibson, *Chem. Commun.*, 2024, **60**, 1876–1879.

65 R. H. A. Jan, C. A. Biji, K. Shakeela, R. R. Shaikh and G. R. Rao, *Catal. Lett.*, 2023, **154**, 1631–1641.

66 C. G. Liu, T. Zheng, S. Liu and H. Y. Zhang, *J. Mol. Struct.*, 2016, **1110**, 44–52.

67 Y. P. Liu, S. F. Zhao, S. X. Guo, A. M. Bond and J. Zhang, *J. Am. Chem. Soc.*, 2016, **138**, 2617–2628.

68 F. C. Shen, C. Guo, S. N. Sun, Z. Lei and Y. Q. Lan, *Inorg. Chem.*, 2022, **61**, 11182–11188.

69 J. M. Xu, Z. G. Zhang, K. Yang, W. W. He, X. D. Yang, X. M. Du, L. X. Meng, P. Y. Zhao and Z. Wang, *J. Membr. Sci.*, 2020, **596**, 15.

70 Q. Chen, D. D. Zhang, M. M. Wang, X. W. Chen and J. H. Wang, *J. Mater. Chem. B*, 2015, **3**, 6964–6970.

71 Y. H. Zhu, J. B. Yang, X. M. Liu, J. L. Wang, Q. D. Ping, Z. Y. Du, J. N. A. Li, T. T. Zang, H. Mei and Y. Xu, *Dalton Trans.*, 2022, **51**, 3502–3511.

72 R. Tian, L. P. Cui, K. Yu, J. H. Lv, Y. J. Ma, L. L. He and B. B. Zhou, *ACS Appl. Nano Mater.*, 2022, **5**, 14882–14892.

73 X. L. Yang, Y. S. Ye, Z. M. Wang, Z. H. Zhang, Y. L. Zhao, F. Yang, Z. Y. Zhu and T. Wei, *ACS Omega*, 2020, **5**, 26230–26236.

74 Y. Du, W. X. Chen, Z. Y. Zhong, S. Z. Wang, L. A. Zhou, D. B. Xiong, Y. S. Liu, Z. H. Liu and K. Wang, *J. Alloys Compd.*, 2023, **960**, 10.

75 X. Q. Li, Z. Wang, C. Y. Hong, F. F. Feng, K. Yu and H. Liu, *Macromolecules*, 2022, **55**, 9583–9593.

76 N. Sun, A. L. Wu, Y. Yu, X. P. Gao and L. Q. Zheng, *Chem.– Eur. J.*, 2019, **25**, 6203–6211.

77 M. Attoui, E. Pouget, R. Oda, D. Talaga, T. Buffeteau and S. Nlate, *Inorg. Chim. Acta*, 2019, **498**, 9.

78 Q. D. Liu and X. Wang, *Angew. Chem., Int. Ed.*, 2023, **62**, e202217764.

79 J. Q. Sha, X. Y. Yang, Y. Y. Chen, P. P. Zhu, Y. F. Song and J. Z. Jiang, *ACS Appl. Mater. Interfaces*, 2018, **10**, 16660–16665.

80 Y. X. Guo, Y. J. Gong, Y. A. Gao, J. H. Xiao, T. Wang and L. Yu, *Langmuir*, 2016, **32**, 9293–9300.

81 J. S. Li, Y. Wang, C. H. Liu, S. L. Li, Y. G. Wang, L. Z. Dong, Z. H. Dai, Y. F. Li and Y. Q. Lan, *Nat. Commun.*, 2016, **7**, 8.

82 K. Xia, K. Yamaguchi and K. Suzuki, *Angew. Chem., Int. Ed.*, 2023, **62**, e202214506.

83 W. J. Luo, J. Hu, H. L. Diao, B. Schwarz, C. Streb and Y. F. Song, *Angew. Chem., Int. Ed.*, 2017, **56**, 4941–4944.

84 T. Wei, M. Zhang, P. Wu, Y. J. Tang, S. L. Li, F. C. Shen, X. L. Wang, X. P. Zhou and Y. Q. Lan, *Nano Energy*, 2017, **34**, 205–214.

85 X. Liu, J. Q. Huang, Q. Zhang and L. Q. Mai, *Adv. Mater.*, 2017, **29**, 1601759.

86 X. Y. Luo, F. J. Li, F. Peng, L. Z. Huang, X. L. Lang and M. Q. Shi, *ACS Appl. Mater. Interfaces*, 2021, **13**, 57803–57813.

87 Y. Hou, J. J. Xin, C. J. Gómez-García, B. X. Xiao, H. J. Pang, H. Y. Ma, X. M. Wang and L. C. Tan, *ACS Appl. Energy Mater.*, 2021, **4**, 13191–13198.

88 Z. H. Liu, L. Yuan, T. P. Wen, J. K. Yu and X. X. Xu, *Int. J. Electrochem. Sci.*, 2023, **18**, 9.

89 Y. K. Lu, X. X. Guo, L. Y. Yang, W. F. Yang, W. T. Sun, Y. X. Tuo, Y. Zhou, S. T. Wang, Y. Pan, W. F. Yan, D. Sun and Y. Q. Liu, *Chem. Eng. J.*, 2020, **394**, 11.

90 M. Guillen-Soler, N. V. Vassilyeva, E. P. Quirós-Díez, J. M. Vila-Fungueiriño, A. Forment-Aliaga and M. D. Gimenez-Lopez, *Adv. Sustainable Syst.*, 2023, **8**, 2300607.

91 Shivaarun, P. Bhartiya, A. Naz, S. Rai, S. S. Narvi and P. K. Dutta, *J. Polym. Mater.*, 2018, **35**, 475–484.

92 A. Joshi, S. Acharya, N. Devi, R. Gupta, D. Sharma and M. Singh, *Nanoscale Adv.*, 2023, **5**, 6045–6052.

93 S. Sun, L. P. Cui, K. Yu, M. L. Wang, J. H. Lv, S. H. Ge and B. B. Zhou, *ACS Appl. Nano Mater.*, 2023, **7**, 1310–1318.

94 W. H. Xie, Y. Ren, F. L. Jiang, X. Y. Huang, B. J. Yu, J. H. Liu, J. C. Li, K. Y. Chen, Y. D. Zou, B. W. Hu and Y. H. Deng, *Nat. Commun.*, 2023, **14**, 9.

95 R. Villanneau, A. Roucoux, P. Beaunier, D. Brouri and A. Proust, *RSC Adv.*, 2014, **4**, 26491–26498.

96 H. K. Kolli, D. Jana and S. K. Das, *Inorg. Chem.*, 2021, **60**, 15569–15582.

97 H. Yang, J. Li, H. Y. Zhang, Y. Lv and S. Gao, *Microporous Mesoporous Mater.*, 2014, **195**, 87–91.

98 Q. Y. Li, L. Zhang, Y. X. Xu, Q. Li, H. G. Xue and H. Pang, *ACS Sustain. Chem. Eng.*, 2019, **7**, 5027–5033.

99 B. X. Xiao, S. U. Khan, G. N. Cui, L. M. Dong, C. J. Zhang, Q. Wu and H. J. Pang, *Clean Technol. Environ.*, 2023, **25**, 2629–2638.

100 C. Singh and S. K. Das, *J. Chem. Sci.*, 2021, **133**, 9.

101 S. F. Li, J. S. Li, H. T. Zhu, L. Y. Zhang, X. J. Sang, Z. M. Zhu, W. S. You and F. X. Zhang, *Dalton Trans.*, 2023, **52**, 15725–15733.

102 Z. F. Zhang, C. J. Gomez-Garcia, Q. Wu, J. J. Xin, H. J. Pang, H. Y. Ma, D. F. Chai, S. B. Li and C. Y. Zhao, *Inorg. Chem.*, 2022, **61**, 11830–11836.

103 J. H. Shi, Z. T. Wang, J. J. Zha, P. S. Wang, P. Wang, X. Y. Jiang, X. Liu, Q. Xu, X. Y. Liu, G. W. Diao and L. B. Ni, *J. Mol. Struct.*, 2024, **1296**, 7.

104 S. Mulkapuri, A. Ravi, R. Nasani, S. K. Kurapati and S. K. Das, *Inorg. Chem.*, 2022, **61**, 13868–13882.

105 S. Mulkapuri, A. Ravi, S. Mukhopadhyay, S. K. Kurapati, V. Siby and S. K. Das, *Inorg. Chem. Front.*, 2022, **9**, 3566–3577.

106 S. Mulkapuri, A. Siddikha, A. Ravi, P. Saha, A. V. Kumar, S. Boodida, M. Vithal and S. K. Das, *Inorg. Chem.*, 2023, **62**, 19664–19676.

107 M. X. Li, Y. Zhang, Z. M. Zhu, F. Su, L. C. Zhang and X. J. Sang, *J. Coord. Chem.*, 2020, **73**, 2437–2449.

108 A. A. Kuznetsova, V. V. Volchek, V. V. Yanshole, A. D. Fedorenko, N. B. Kompankov, V. V. Kokovkin, A. L. Gushchin, P. A. Abramov and M. N. Sokolov, *Inorg. Chem.*, 2022, **61**, 14560–14567.

109 P. Sood, A. Joshi and M. Singh, *Nanoscale Adv.*, 2022, **4**, 5015–5020.

110 K. Azmani, M. Besora, J. Soriano-López, M. Landolsi, A. L. Teillout, P. de Oliveira, I. M. Mbomekallé,

J. M. Poblet and J. R. Galán-Mascarós, *Chem. Sci.*, 2021, **12**, 8755–8766.

111 N. Hu, J. Du, Y. Y. Ma, W. J. Cui, B. R. Yu, Z. G. Han and Y. G. Li, *Appl. Surf. Sci.*, 2021, **540**, 10.

112 A. Kar, L. Sharma, A. Kumar, A. Halder and C. P. Pradeep, *Eur. J. Inorg. Chem.*, 2022, **2022**, 12.

113 K. Li, S. Zhang, K. L. Zhu, L. P. Cui, L. Yang and J. J. Chen, *J. Am. Chem. Soc.*, 2023, **145**, 24889–24896.

114 H. M. Zeng, Z. G. Jiang, H. W. Zhang, W. T. Mao, X. H. Gao and C. H. Zhan, *Eur. J. Inorg. Chem.*, 2021, **2021**, 2606–2610.

115 Q. Huang, Q. Niu, X. F. Li, J. Liu, S. N. Sun, L. Z. Dong, S. L. Li, Y. P. Cai and Y. Q. Lan, *Sci. Adv.*, 2022, **8**, 13.

116 J. J. Fang, Z. Liu, Y. L. Shen, Y. P. Xie and X. Lu, *Chem. Sci.*, 2023, **14**, 12637–12644.

117 M. T. Peng, C. Chen, Y. Zhang, J. Y. Xu, Y. L. Teng and B. X. Dong, *Dalton Trans.*, 2023, **52**, 10737–10743.

118 L. Yu and Q. Liang, *New J. Chem.*, 2022, **46**, 3073–3077.

119 Y. Tang, Z. J. Zou, X. G. Wu, P. F. Zuo, L. Wang, G. W. Huang, J. Zhu and S. L. Zhong, *New J. Chem.*, 2023, **47**, 9887–9893.

120 H. Zhou, Y. Y. Dong, X. Xin, M. Z. Chi, T. L. Song and H. J. Lv, *J. Mater. Chem. A*, 2022, **10**, 19963–19971.

121 M. Zhang, H. J. Li, J. H. Zhang, H. J. Lv and G. Y. Yang, *Chin. J. Catal.*, 2021, **42**, 855–871.

122 Y. Q. Feng, L. Qin, J. H. Zhang, F. Y. Fu, H. J. Li, H. Xiang and H. J. Lv, *Chin. J. Catal.*, 2022, **43**, 442–450.

123 D. Y. Jin, F. Qiao, Y. Zhou, J. F. Wang, K. C. Cao, J. Yang, J. K. Zhao, L. Zhou and H. T. Li, *Nano Res.*, 2023, **17**, 2546–2554.

124 F. Yang, R. Q. Yao, Z. L. Lang, F. Y. Yu, H. L. Dong, Y. H. Wang, Y. G. Li and H. Q. Tan, *ACS Energy Lett.*, 2023, **8**, 5175–5183.

125 Y. Hou, H. J. Pang, J. J. Xin, H. Y. Ma, B. N. Li, X. M. Wang and L. C. Tan, *Adv. Mater. Interfaces*, 2020, **7**, 9.

126 S. B. Li, J. W. Liang, X. G. Tan, F. B. Li, X. M. Wang, L. Ma, L. Zhang and K. Cheng, *Int. J. Hydrogen Energy*, 2024, **51**, 1128–1137.

127 X. Y. Che, H. J. Pang, S. M. Hu, T. T. Yu, Z. X. Jin, Q. F. Zhen, H. Y. Ma, M. X. You and C. J. Zhang, *Inorg. Chem. Commun.*, 2023, **155**, 9.

128 Z. X. Jin, H. J. Pang, K. Q. Li, M. L. Yang, J. J. Xin, H. Y. Ma, Q. Wu, X. M. Wang and G. X. Yang, *ChemNanoMat*, 2023, **10**, e202300358.

129 T. C. Shi, L. Men, X. H. Zhen, X. Li, J. Li, D. M. Wang and Z. M. Su, *New J. Chem.*, 2023, **47**, 21937–21943.

130 S. Pathan, M. Ankitha, A. A. Mohan, N. Shabana, Y. Tong and P. A. Rasheed, *Mater. Adv.*, 2024, **5**, 274–281.

131 Y. Yang, L. J. Liu, S. Chen, W. J. Yan, H. Q. Zhou, X. M. Zhang and X. J. Fan, *Angew. Chem., Int. Ed.*, 2023, **62**, e202306896.

132 M. L. Hu, Z. N. Wang, M. L. Li, K. M. Pan and L. P. Li, *Int. J. Hydrogen Energy*, 2021, **46**, 28087–28097.

133 I. Sakthinathan, J. Koehling, V. Wagner and T. McCormac, *ACS Appl. Mater. Interfaces*, 2023, **15**, 2861–2872.

134 C. L. Yue, Y. Zhou, Y. Liu, C. Feng, W. J. Bao, F. Y. Sun, Y. X. Tuo, Y. Pan, Y. Q. Liu and Y. K. Lu, *Inorg. Chem. Front.*, 2022, **9**, 2617–2627.

135 C. H. Ma, S. S. Zhu, Y. C. Zhao, X. Y. Wang, T. Z. Zhan, L. H. Chen, J. N. Wang, Q. Ling, Z. C. Xiao, X. F. Wu, J. L. Cai and P. F. Wu, *Langmuir*, 2023, **40**, 744–750.

136 A. Joshi, P. Sood, A. Gaur, D. Rani, V. Madaan and M. Singh, *J. Mater. Chem. A*, 2022, **10**, 12805–12810.

137 Y. Zhang, H. R. Guo, J. K. Ren, X. P. Li, W. L. Ren and R. Song, *Appl. Catal., B*, 2021, **298**, 9.

138 K. F. Shi, Z. M. Sun, M. W. Yuan, Y. L. Zhao and G. B. Sun, *J. Colloid Interface Sci.*, 2024, **657**, 37–45.

139 Y. Li, X. R. Chang, X. J. Sang, J. S. Li, Y. H. Luo, Z. M. Zhu and W. S. You, *Eur. J. Inorg. Chem.*, 2019, **2019**, 3597–3604.

140 H. Liu, L. G. Gong, C. X. Wang, C. M. Wang, K. Yu and B. B. Zhou, *J. Mater. Chem. A*, 2021, **9**, 13161–13169.

141 Y. P. Zhao, D. D. Gao, S. Liu, J. Biskupek, U. Kaiser, R. J. Liu and C. Streb, *Chem.–Eur. J.*, 2023, **29**, e202203220.

142 S. Mukhopadhyay, O. Basu, A. Kar and S. K. Das, *Inorg. Chem.*, 2020, **59**, 472–483.

143 V. K. Abdelkader-Fernández, D. M. Fernandes, S. S. Balula, L. Cunha-Silva and C. Freire, *ACS Appl. Energy Mater.*, 2020, **3**, 2925–2934.

144 V. K. Abdelkader-Fernández, D. M. Fernandes, S. S. Balula, L. Cunha-Silva and C. Freire, *J. Mater. Chem. A*, 2020, **8**, 13509–13521.

145 S. Mulkapuri, A. Ravi and S. K. Das, *Chem. Mater.*, 2022, **34**, 3624–3636.

146 J. X. Song, P. F. Zhu, W. M. Ma and Y. X. Li, *Int. J. Hydrogen Energy*, 2024, **51**, 327–337.

147 T. Ahmed, M. A. Asghar, A. Ali, Z. Akhter, S. Ali, I. Ullah, T. Nisar, V. Wagner, S. Touseef, A. Hussain and A. Haider, *J. Alloys Compd.*, 2022, **909**, 7.

148 C. Lee, D. Jeon, J. Park, W. Lee, J. Park, S. J. Kang, Y. Kim and J. Ryu, *ACS Appl. Mater. Interfaces*, 2020, **12**, 32689–32697.

149 R. H. Gong, D. D. Gao, R. J. Liu, D. Sorsche, J. Biskupek, U. Kaiser, S. Rau and C. Streb, *ACS Appl. Energy Mater.*, 2021, **4**, 12671–12676.

150 V. K. Abdelkader-Fernández, D. M. Fernandes, L. Cunha-Silva, A. J. S. Fernandes and C. Freire, *Electrochim. Acta*, 2021, **389**, 12.

151 Y. Q. Feng, F. Y. Fu, L. L. Zeng, M. Y. Zhao, X. Xin, J. K. Liang, M. Zhou, X. K. Fang, H. J. Lv and G. Y. Yang, *Angew. Chem., Int. Ed.*, 2024, **63**, e202317341.

152 M. L. Sun, Y. R. Wang, W. W. He, R. L. Zhong, Q. Z. Liu, S. Y. Xu, J. M. Xu, X. L. Han, X. Y. Ge, S. L. Li, Y. Q. Lan, A. M. Al-Enizi, A. Nafady and S. Q. Ma, *Small*, 2021, **17**, 2100762.

153 H. Z. Yang, D. R. Yang, Y. Zhou and X. Wang, *J. Am. Chem. Soc.*, 2021, **143**, 13721–13730.

154 J. Du, Z. L. Lang, Y. Y. Ma, H. Q. Tan, B. L. Liu, Y. H. Wang, Z. H. Kang and Y. G. Li, *Chem. Sci.*, 2020, **11**, 3007–3015.

155 W. C. Sun, D. Yao, Y. H. Tai, L. Zhou, W. X. Tian, M. Yang and C. X. Li, *J. Colloid Interface Sci.*, 2023, **650**, 121–131.

156 B. J. Zha, C. X. Li and J. J. Li, *J. Catal.*, 2020, **382**, 69–76.

157 D. J. Zang, Q. Li, G. Y. Dai, M. Y. Zeng, Y. C. Huang and Y. G. Wei, *Appl. Catal., B*, 2021, **281**, 13.

13604 | *J. Mater. Chem. A*, 2024, **12**, 13576–13604

This journal is © The Royal Society of Chemistry 2024